Friction Mediates Scission of Tubular Membranes Scaffolded by BAR Proteins

Friction Mediates Scission of Membrane Nanotubes Scaffolded by BAR Proteins

Mijo Simunovic[1,2,3,a], Jean-Baptiste Manneville[4‡], Henri-François Renard[5‡,b], Emma Evergren[6,7], Krishnan Raghunathan[8], Dhiraj Bhatia[5], Anne K. Kenworthy[8], Gregory A. Voth[3], Jacques Prost[1,2,9], Harvey T. McMahon[6], Ludger Johannes[5], Patricia Bassereau[1,2*c], Andrew Callan-Jones[10*]

1. Laboratoire Physico Chimie Curie, Institut Curie, PSL Research University, CNRS UMR168, 75005 Paris, France
2. Sorbonne Universités, UPMC Univ Paris 06, 75005 Paris, France
3. Department of Chemistry, Institute for Biophysical Dynamics, James Franck Institute and Computation Institute, The University of Chicago, 5735 S Ellis Avenue, Chicago, IL 60637, USA
4. Institut Curie, PSL Research University, Subcellular Structure and Cellular Dynamics unit, CNRS UMR144, 75005 Paris, France
5. Institut Curie, PSL Research University, Chemical Biology of Membranes and Therapeutic Delivery unit, CNRS UMR3666, INSERM U1143, 75248 Paris Cedex 05, France
6. Medical Research Council Laboratory of Molecular Biology, Francis Crick Avenue, Cambridge CB2 0QH, UK
7. Centre for Cancer Research and Cell Biology, Queen's University Belfast, Belfast, UK
8. Vanderbilt School of Medicine, Department of Molecular Physiology and Biophysics, 718 Light Hall, Nashville, TN 37232, USA.
9. Mechanobiology Institute, National University of Singapore, Singapore
10. CNRS, Laboratoire Matière et Systèmes Complexes, UMR 7057, Paris, France

*corresponding authors: (lead contact) patricia.bassereau@curie.fr, andrew.callan-jones@univ-paris-diderot.fr
‡: equally contributing authors

Current addresses
[a] Center for Studies in Physics and Biology, The Rockefeller University, 1230 York Avenue, New York, USA
[b] Institut des Sciences de la Vie, Université catholique de Louvain, B1348 Louvain-la-Neuve, Belgium
[c] Lead contact

SUMMARY

Membrane scission is essential for intracellular trafficking. While BAR domain proteins such as endophilin have been reported in dynamin-independent scission of tubular membrane necks, the cutting mechanism has yet to be deciphered. Here, we combine a theoretical model, *in vitro*, and *in vivo* experiments revealing how protein scaffolds may cut tubular membranes. We demonstrate that the protein scaffold bound to the underlying tube creates a frictional barrier for lipid diffusion; tube elongation thus builds up local membrane tension until the membrane undergoes scission through lysis. We call this mechanism friction-driven scission (FDS). In cells, motors pull tubes, in particular during endocytosis. Through reconstitution, we show that motors can not only pull out and extend protein-scaffolded tubes, but also cut them by FDS. FDS is generic, operating even in the absence of amphipathic helices in the BAR domain, and could in principle apply to any high friction, protein/membrane assembly.

KEYWORDS

Endocytosis; membrane scission; membrane tube; BAR domain; endophilin; scaffold; friction-driven scission; diffusion barrier; in vitro reconstitution; molecular motors; pore nucleation

HIGHLIGHTS

- BAR protein scaffolds form a lipid diffusion barrier on membrane nanotubes
- Elongation force on tubes reveals scaffold-membrane friction
- Local tension rises due to friction, leading to pore nucleation and tube scission
- Microtubule-associated molecular motors pull and cut scaffolded tubes

INTRODUCTION

Endocytosis allows cells to internalize nutrients and proteins, and is also used by pathogens in the course of infection (McMahon and Boucrot, 2011). While clathrin-mediated endocytosis (CME) has been investigated for many years (Kirchhausen et al., 2014; Merrifield and Kaksonen, 2014; Schmid et al., 2014), clathrin-independent endocytoses (CIE) have begun only recently to be revealed (Johannes et al., 2015; Soykan et al., 2016). Scission, the process of detachment of the endocytic bud from the plasma membrane, differs between CME and CIE. In CME in mammalian cells, scission requires the assembly of dynamin at the neck of the vesicle, and it can be assisted by actin polymerization (Boulant et al., 2011; Ferguson et al., 2009) and Bin/Amphiphysin/Rvs (BAR) proteins (Meinecke et al., 2013; Neumann and Schmid, 2013; Sundborger et al., 2011; Yoshida et al., 2004). In CIE, which typically involves tubular membrane structures, scission appears to require a more equal division of labor between these three proteins (Renard et al., 2015).

In both CME and CIE, a number of scission modules may coexist in a single endocytic pathway, rendering the process more robust, although obscuring the underlying mechanisms. In the most prominent scission mechanism, dynamin polymerizes at the neck of the clathrin vesicle or on a tubular tether, then tightens it upon GTP hydrolysis until it breaks (Morlot et al., 2012; Roux et al., 2006; Shnyrova et al., 2013). However, scission may take place in the absence of nucleotide hydrolysis. Line tension at the edge of lipid domains can generate enough constriction to drive spontaneous vesiculation or scission of tubes (Allain et al., 2004; Romer et al., 2010). In yeast, it may be assisted by forces exerted by actin polymerization (Liu et al., 2006). Finally, shallow insertion of amphipathic helices (AHs) into the bilayer may also lead to scission of small vesicles, as observed in the case of epsin and N-BAR proteins (Boucrot et al., 2012; Simunovic et al., 2013).

Direct *in vitro* evidence of scission of preformed membrane tubes by N-BAR proteins has not been observed under static conditions, indicating a possible difference between scission mechanisms of spherical and tubular membranes. Our *in vitro* pilot study showed that endoA2-scaffolded tubes undergo scission when extended by an external force in CIE (Renard et al., 2015). Although dynein molecular motors walking on microtubules have been shown to be crucial for tube elongation during CIE *in vivo* (Day et al., 2015), the scission mechanism and the role of molecular motors remain unknown.

Here, we combine a minimal experimental system and devise a theoretical model to describe this unexplored scission mechanism. We demonstrate that friction between a BAR protein scaffold and an elongated membrane tube increases membrane tension up to tube rupture upon elongation. Our experiments allow us to discriminate our proposed scission model from existing ones, namely pinching via hemifission or constriction by line tension, thus identifying the minimal components needed to cut membrane tubes stabilized by BAR protein scaffolds. We term the mechanism friction-driven scission (FDS) and demonstrate that motor proteins provide the necessary elongation force in the cell.

RESULTS

External elongation force induces scission of endophilin-scaffolded tubes

We first studied if BAR-domain proteins may induce scission of flat or tubular membranes. We considered two BAR proteins: endophilin A2 (endoA2) or its N-BAR domain alone, containing four AHs, and β2 centaurin (centaurin), containing no AHs. As models of the cell membrane we created (1) giant unilamellar vesicles (GUVs), (2) tensed supported bilayers,

and (3) tensionless membrane sheets. GUVs were composed of the total brain lipid extract supplemented with 5% PI(4,5)P_2 (mol/mol). Consistent with previous findings (Peter et al., 2004; Sorre et al., 2012; Takei et al., 1999), both proteins at 1–5 μM concentrations induced spontaneous tubulation, with no evidence of scission (Figure S1; Movie S1). To see if BAR proteins cut cylindrical membranes, mimicking tubular membrane transport intermediates, we pulled tubes from GUVs using optical tweezers. The tube-pulling force, f, can be measured while the tube radius, r, and vesicle tension, σ_v, can be controlled (see STAR Methods). Under a wide range of σ_v (0.001–0.4 mN.m^{-1}) and r (10–120 nm), these proteins stabilized membrane tubes by forming a scaffold and in a vast majority of cases they did not cut them (see SI for more details).

Nevertheless, there is evidence that endoA2-coated tubes can be cut upon elongation (Renard et al., 2015). Elongation has little effect on the force and stability of a bare membrane tube when pulled at biologically relevant speeds (Evans and Yeung, 1994), however the presence of a protein scaffold might have a significant mechanical effect, potentially even to destabilize the tube. As a control, we elongated protein-free tubes at speeds up to 20 μm.s^{-1} and observed no scission. We measured only modest elongation-dependent force changes (Figure S2), consistent with (Evans and Yeung, 1994). We then elongated protein-scaffolded membrane tubes. We injected endoA2 near the pulled tube, which forms a scaffold partially or along the whole length of the tube stabilizing it (Simunovic et al., 2016). Then, we extended the tube at constant speed V by displacing the aspirated GUV away from the optical trap. The tube-pulling force increased significantly upon tube extension until it dropped suddenly to zero, suggesting scission (Figure 1A). Scission was clearly observed by time-lapse confocal imaging of lipid and protein fluorescence (Figure 1B,C). In the case of endoA2, scission took place in 93% of the experiments (N = 43) at V = 50–8000 nm.s^{-1} (Figure 1 and Movies S2 and S3). Elongation at 20 nm.s^{-1} resulted in a very slow increase in f with no scission in 150 s of the experiment (Figure S3).

Confocal imaging of partially scaffolded tubes demonstrated that, during extension, the protein scaffold moved together with the displaced GUV, away from the fixed bead, indicating that the scaffold is mechanically connected to the vesicle (Figure 1B). It also showed that the tube radius remained unchanged under pulling (Figure S4). The relative movement between the scaffold and the membrane tube will be important in building a theoretical model and explaining the mechanism of membrane scission.

To see whether extension-driven tube scission is specific to endoA2-scaffolded tubes and the importance of AHs in this process, we considered centaurin and two endophilin mutants: one in which we truncated the N-terminal AHs (endoA2 ΔH0) and on in which we mutated a glutamate and an aspartate from the membrane-binding region of the N-BAR domain into lysines (E37K, D41K) (endoA2 mut). This reversal of charge enhances the binding strength of the BAR domain backbone to the membrane. Both mutants assemble into scaffolds on tubes, as we have recently shown (Simunovic et al., 2016). While it has been recently shown that helix deletion does not impair the protein's curvature-generating ability (Chen et al., 2016), scaffold formation requires 7x higher bulk protein concentration (Simunovic et al., 2016). We observed scission in all experiments for endoA2 ΔH0 (N = 6), in agreement with (Renard et al., 2015), and in 92% of experiments for endoA2 mut (N = 13; in the only negative case, the bead was ejected from the trap). Finally, we observed five scission events upon elongation of centaurin-scaffolded tubes (N = 8; in the three negative cases the bead was ejected). In conclusion, BAR proteins do not cut static membrane tubes; rather,

they cut dynamically extended tubes via a mechanism that is not specific to the BAR protein backbone or the presence of AHs.

Endophilin scaffold forms a lipid mobility barrier.

Our observations that the force increases when scaffolded tubes are extended suggest a role for friction between the scaffold and the underlying tube in scission. In a different context, a force increase upon pulling tubes with transmembrane proteins or contaminants has been attributed to an augmented friction between the bilayer leaflets (Callan-Jones et al., 2016; Campillo et al., 2013). This scaffold-tube friction is expected to reduce lipid diffusion in the tube. To test this hypothesis, we monitored the fluorescence recovery after photobleaching (FRAP) of the entire tube. If the mobility of the bleached component is unperturbed, the fluorescence rapidly recovers due to the mixing of the bleached and the unbleached markers. As expected, the fluorescence recovery of protein-free tubes was fast (<5 s) (Figure 2A), consistent with the recovery time for free lipids in a tube (Berk et al., 1992). Conversely, in the presence of a scaffold formed by the N-BAR domain of endoA2, there was essentially no recovery, even after 90 s (Figure 2A). Note that the weak decrease of the lipid diffusion coefficient on protein-free tubes with decreasing tube radius (Domanov et al., 2011) cannot account for this dramatic change. This reduction in lipid mobility is consistent with high friction between tubular lipids and the surrounding protein scaffold (Merkel et al., 1989).

Another way to detect the influence of the scaffold on lipid mobility is by measuring the change in r resulting from a change in vesicle tension, σ_{v}. For a protein-free tube, r adjusts within seconds after a σ_{v} change (Dommersnes et al., 2005). We considered a partially scaffolded tube, in which the scaffold was located between the protein-poor part of the tube and the GUV. When the vesicle tension was increased step-wise, with a waiting period of about a minute between steps, there was no detectable change in the protein-free r, as measured by lipid fluorescence (Figure 2B). This observation suggests that the tension in the protein-free tube was not equilibrated with the vesicle, likely as a result of the friction between the scaffold and the tube lipids.

Modeling friction between a protein scaffold and a membrane tube

Our measurements of the increasing force as scaffolded tubes are extended and the reduction in lipid mobility detected by FRAP suggest that friction opposes the relative movement between the scaffold and the underlying membrane. Below, we model this hypothesis, and test it against our force measurements.

When protein-scaffolded tubes were extended at constant velocity V (schematized in Figure 3A), we found that the force, $f(t)$, increased at short times after extension began, and then tended to a constant value (Figures 1A, 3B). The saturating force, f_∞, increased with V (Figure 3B). These observations suggest a viscoelastic-like response: at short times the behavior is elastic, as lipid flow from the vesicle to the tube is impeded by friction, and f increases due to the stretching of the tubular membrane. At longer times, a balance between tube extension and lipid influx underneath the scaffold sets in, the force becomes constant and friction dominates.

We consider at time t a tube of length $L_{\mathrm{tube}}(t)$ coated with a protein scaffold of fixed radius r_{s}. Since tubes were often found to be incompletely coated (Figure 1B), the total length is written $L_{\mathrm{tube}}(t) = L_{\mathrm{s}} + L(t)$, where L_{s} and $L(t)$ are the lengths of scaffolded and un-scaffolded tubes (Figure 3A). The un-scaffolded tube is expected to be cylindrical, with radius $r(t)$, at distances of the order r away from the scaffold interface (Morlot et al., 2012).

In cases where tubes appeared to be initially fully covered, we often observed that almost immediately after extension began, gaps in the scaffold appeared (Figure S5). This effectively renders the tubes incompletely coated for most of the extension period, and our hypothesis of partially coated tubes is generally valid. Upon extension, we assume, in agreement with experimental observations, that the scaffold is rigid and does not change its length (Figure 1C), and therefore $L(t) = L_0 + \Delta L(t)$, with L_0 the initial length of uncoated tube and $\Delta L(t)$ the controlled change in tube length. For constant speed extension $\Delta L(t) = Vt$ and for a sudden step, $\Delta L(t) = \Delta L_{\text{step}}$.

A key ingredient in the model is that elongation of a scaffolded tube causes an increase in tube tension, an effect that does not occur for bare membrane tethers (Derenyi et al., 2002). Adapting a model of tether pulling from cytoskeleton-attached membranes (Brochard-Wyart et al., 2006), friction dynamically relates the tube tension $\sigma(t)$ to the speed, v_{l}, of lipids underneath the scaffold:

$$\sigma(t) = \sigma_0 + \xi\, v_{\text{l}} \tag{1}$$

where σ_0 is the tension before extension begins and ξ is the scaffold-membrane friction coefficient. This friction reflects dissipation due to relative movement between membrane lipids and proteins forming the scaffold (see Figure 3A). Equation 1 is an integrated expression of the linear momentum conservation law in the lipid layer (see SI for a detailed discussion).

The increase in tension due to friction leads to a change in the tube pulling force, which can be measured directly. Noting that lipid membranes are practically incompressible (Rawicz et al., 2000), which implies $d(rL)/dt = r_{\text{s}} v_{\text{l}}$, and using known relations between r , f, and σ for the un-scaffolded tube (Derenyi et al., 2002), it can be shown (SI) that Equation 1 leads to:

$$\frac{d}{dt}\left(\frac{L}{f}\right) = \frac{f^2 - {f_0}^2}{16\pi^2\kappa^2\xi/r_{\text{s}}}\,. \tag{2}$$

This equation can be solved for *f(t)* for the experimental protocols for *L(t).*

By applying our model to $f(t)$ for endoA2-scaffolded tubes, we were able to estimate the friction coefficient ξ. Moreover, since endoA2 mutants interact differently with the membrane than does endoA2 WT, we expect that ξ reflects these differences. Solving equation (2) for $L(t) = L_0 + Vt$ yields an explicit expression for *f(t)*:

$$f(t) = f_0 \frac{1 + Vt/L_0}{\left(1 + \frac{(1+Vt/L_0)^3}{16\pi^3\kappa^2\xi V/(r_{\text{s}}{f_0}^3)}\right)^{1/3}}\,; \tag{3}$$

see Figure 3C for the variation of *f* with *t*. Note that the above equation is valid as long as $V \gg r_{\text{s}}{f_0}^3/(16\,\pi^3\kappa^2\xi)$; see SI. In practice, as discussed below, this equality requires that $V \gtrsim 50$ nms^{-1}, which is always the case.

Equation (3) recapitulates the viscoelastic-like properties announced earlier, revealing two distinct regimes. At times short compared with

$$t^* = \left(\frac{16\pi^3\kappa^2\xi{L_0}^3}{r_{\text{s}}{f_0}^3 V^2}\right)^{1/3} \tag{4}$$

the tube is elongated elastically at fixed number of lipids, and the force increases linearly with t with slope $f_0 V/L_0$; while for times greater than t^*, lipid influx across the scaffold occurs and the force saturates to

$$f_\infty \approx \left(\frac{16\pi^3\kappa^2\xi}{r_s}\right)^{1/3} V^{1/3} . \quad (5)$$

In addition, the tension in the tube builds up to $\sigma_\infty = {f_\infty}^2/(8\pi\kappa) \propto (\xi V)^{2/3}$. Thus, our proposed scission mechanism via tension-caused membrane pore nucleation (see below) is seen to depend crucially on friction and pulling speed.

Our model allows us to quantitatively determine the effects of protein scaffolding on tube dynamics. The *f vs t* data for endoA2 WT-scaffolded tubes were first obtained by performing several elongation experiments (*N*=10) (Figure 3B). For each experiment, the pulling speed *V* was held constant; *V* ranged from 50 nm.s^{-1} to >5 μm.s^{-1}. Fitting these data sets with equation 3 allowed us to determine an average friction coefficient, ξ (Figure 3D). From the data, we note that, with increasing *V*, *f* rose faster and at long time, saturated at higher f_∞ values, in agreement with the model prediction (Figure 3C).

As an independent test of our model, we performed a force relaxation experiment on a WT-scaffolded tube, in which the length of the tube was increased stepwise and the subsequent force behavior was monitored (Figure 3E). Fitting the force relaxation after two steps (Figure 3F) by solving equation 2 (see SI for details) yields good agreement with the constant speed elongation experiments. Thus, the friction between a protein scaffold and a membrane tube is a general mechanical property of dynamic tubes. It provides a quantitative measure of the scaffold's ability to create a local tension increase on the tube, which as we show, is a pre-requisite for scission.

A further validation of the model was found by comparing the ways in which endoA2 WT and two mutants, endoA2 ΔH0 and endoA2 mut, affect the tube force. For comparable elongation speeds, *f* attains a lower saturation force for endoA2 ΔH0 (Figure 3G) than for WT (Figure 3B), whereas *f* tends to a slightly higher value for endoA2 mut (Figure 3H). Based on our theoretical model (Figure 3I), these trends suggest that the friction between an endoA2 ΔH0 scaffold and the lipid tube is lower than for WT, and greater for endoA2 mut scaffold, confirmed by fitting the data for the two mutants (Figure 3D). This is consistent with the effect of insertion of AHs shown in (Ambroso et al., 2014), and suggests a correlation between binding affinity and friction. As we show now, this scaffold friction-generated force increase provides a natural mechanism to cut tubes, which we refer to as Friction-Driven Scission (FDS). Box 1 presents a summary of the FDS mechanism.

Nucleation of pores in the membrane causes rupture of membrane tubes through FDS.

Three routes to scission of membrane tubes can be considered. First, local tube pinching from a radius r_0 down to $r_i \approx 3$ nm leads to scission via a hemifission intermediate state (Kozlovsky and Kozlov, 2003). Second, it has been proposed that line tension, which arises at the boundary between lipid domains and acts to reduce the boundary length, could constrict tubes enough to cause scission (Allain et al., 2004; Romer et al., 2010). The characteristic scission times of a endoA2-scaffolded tube by each of these mechanisms can be estimated, and are orders of magnitude larger than what we have measured; see SI for details. In the last route, scission is preceded by the nucleation and growth of a pore in membrane at lysis

tension, a process which has been studied extensively in synthetic membrane systems (Evans et al., 2003). In our case, we have shown that scaffold friction leads to a force increase, and so a tension increase in the bare membrane tube upon elongation. Assuming a tube extension rate of 1 μm.s^{-1}, the tension increases roughly at 0.1 mN.m^{-1}.s^{-1}; according to (Evans et al., 2003), this loading rate corresponds to a lysis tension of about 1 mN.m^{-1}, and a tube lysis force of about 100 pN. This value is on the order of magnitude of the force attained in our extension experiments (Figure 3), indicating that scission through membrane lysis is a plausible mechanism of FDS.

In order to test our hypothesis of FDS, we now investigate in detail how the scission force and rupture time depend on the extension rate, as illustrated in Figure 4A. When extended at constant speed V, endoA2-coated tubes broke at a time t_{break} that was found to decrease with increasing V (Figure 4B). Furthermore, tube breaking appears to be a stochastic process. These combined observations suggest that tube scission involves thermal activation over a barrier that is lowered by the applied force.

To model this effect, we assume heterogeneous membrane pore nucleation at a scaffold edge, either along the tube, at the GUV neck, or at the tube end, since most tubes were found to break at these locations (Movies S2 and S3). Nucleation of a roughly semicircular-shaped pore of radius r_{s} is energetically opposed by forming a free membrane edge, with edge tension γ, but is favored by releasing bending and stretching energy (Figure 4A). As can be shown (see SI), these considerations lead to an energy barrier $W(t) \simeq \pi\,\gamma r_{\mathrm{s}} - r_{\mathrm{s}}^{2}\, f(t)^2/8\pi\kappa$, which is elongation speed-dependent. The probability, $P(t)$, for nucleation of a pore of size r_{s} at time t after elongation begins can then be related to W using Kramers' theory for thermally-activated escape (Kramers, 1940); see SI for details. Following (Evans et al., 2003), the scission time, t_{break}, is identified with the peak of $P(t)$. This leads to analytical expressions for t_{break} in the limits $t_{\mathrm{break}} \gg t^*$ and $t_{\mathrm{break}} \ll t^*$, i.e., for slow and fast pulling; see inset of Figure 4B in which the crossover between the regimes is found to occur for $V \sim 1$ μm.s^{-1}. In the limit $t_{\mathrm{break}} \gg t^*$ we obtain

$$t_{\mathrm{break}} \simeq \tau \exp\left[-\frac{\pi}{k_{\mathrm{B}}T}\left(\frac{\kappa\xi^2 r_{\mathrm{s}}^{4}\, V^2}{128}\right)^{1/3}\right], \qquad (6)$$

where τ depends algebraically on V, and thus the dependence of t_{break} on V is dominated by the exponential. Representing the endoA2 WT data as $\ln(t_{\mathrm{break}})$ *vs* $V^{2/3}$ reveals the two pulling regimes (Figure 4B). By performing a linear fit at low pulling speeds, we obtain another determination of the friction coefficient (Figure 4C), in good agreement with earlier values (Table 1). This result strongly supports our model of FDS through pore nucleation.

The dependence of the tube force at scission, $f_{\mathrm{break}} = f(t_{\mathrm{break}})$, on pulling speed provides a second test of FDS. For $t_{\mathrm{break}} \gg t^*$, the force is essentially saturated and therefore, according to equation 5, the extra force provided by tube elongation until scission is $\Delta f \equiv f_{\mathrm{break}} - f_0 \sim (16\pi^3\kappa^2\xi/r_{\mathrm{s}})^{1/3} V^{1/3}$. This prediction is borne out well by our data (Figure 4D, E). In addition, a fit of Δf versus $V^{1/3}$ at low V was done to obtain the friction coefficients for endoA2 WT, endoA2 ΔH0, and endoA2 mut (Figure 4F). We see that two separate analyses—fitting *f(t)* and f_{break} — show the same effect of mutation on the friction coefficient, further confirming the validity of the scission model; see Table 1 and further discussion in SI on the different determinations of ξ.

Molecular motors and BAR proteins induce scission.

Tube elongation in cells is often mediated by molecular motors. Motors walking on microtubules *in vitro* can extract membrane tubes at speeds ranging from a few tens to a few hundred nm.s^{-1} per second (Leduc et al., 2004). Higher speeds, close to one μm.s^{-1}, have been observed *in vivo* (Sciaky et al., 1997; Skjeldal et al., 2012), exceeding the pulling speed of ~50 nm.s^{-1} that we found was needed for FDS. Considering that dynein was shown to elongate Shiga or Cholera toxin-containing tubular membranes under low-ATP conditions in CIE (Day et al., 2015; Renard et al., 2015), we tested if this motor can pull tubes quickly enough to trigger FDS.

First, we confirmed that dynein drives the elongation of tubes containing Shiga toxin subunit B (STxB) in CIE under normal ATP levels in cells (SI and Figure S6A). Then, to measure the tube-pulling rates *in vivo*, we tracked the motion of tubes containing Cholera toxin subunit B (CTxB) on live-cell imaging data published in (Day et al., 2015). Kinematic analysis (see STAR Methods) revealed that the extension speed of dynein-pulled tubes in low-ATP conditions was <50 nm.s^{-1} with the longest tubes extending at <20 nm.s^{-1} (only 7 out of 228 time segments from a total of 25 tubules reached speeds >50 nm.s^{-1}, and never >90 nm.s^{-1}) (Figure 5A,B, Figure S6B). Two observations can be made: (1) under normal ATP conditions, motors most likely exceed the "threshold" velocity of 50 nm.s^{-1} and (2) not observing tubes pulled at high speeds may indicate they have been cut.

To directly observe FDS by motor proteins, we devised a biomimetic system combining GUVs, endoA2 and kinesin motors. Kinesins were previously shown to pull out tubes from GUVs *in vitro* (Koster et al., 2003; Leduc et al., 2004; Roux et al., 2002). We first confirmed that kinesin successfully extracted tubes from GUVs composed of lipids used in this study (see STAR Methods) (Figure 5C and Figure S6D). Next, during tube extension by motors, we injected endoA2 into the system, which quickly became enriched on motor-pulled tubes. Seconds later, we observed scission (four observations in three experiments) (Figure 5D, Figure S6E, and Movies S4 and S5). We quantified these scission events by comparing the prevalence of motor-pulled tubes from GUVs in the presence and absence of endoA2 at 30 min post incubation (Figure 5E). In the presence of endoA2, the number of GUVs with long tubes as well as the number of tubes per GUV decreased more than two-fold. Furthermore, motor-pulled tubes were almost twice as short in the presence of endoA2 (Figure 5E). This further confirms that motors work with endoA2 to induce scission. We note that endoA2 alone induces tubulation of GUVs (Figure S1A); therefore, observing fewer tubes in the presence of endoA2 and motors strengthens the conclusion that their pulling velocity is sufficient to induce scission. Interestingly, we also observed fewer branches, likely indicating that tubes broke from networks and not just from the GUVs.

To summarize, molecular motors extending tubes at speeds of a few tens to hundreds of nm.s^{-1} can provide the force needed to cause scission. Under physiological conditions, it is expected that higher tube extension speeds are achievable, and thus motor-aided scission events are even more prevalent.

DISCUSSION

Scission of membrane invaginations is an essential component of endocytosis and intracellular trafficking. While a number of membrane-bound trafficking factors have been identified in scission (e.g. dynamin, endophilin and actin), a global, mechanistic understanding of how they function has remained elusive, with the notable exception of

dynamin-driven neck constriction. FDS is a generic mechanism and requires that the tube-bound proteins impose a strong friction onto the underlying membrane. It also requires two mechanical conditions: (1) an external force elongating the tube, and (2) an anchoring of the protein structure at the tube base. In the case of CIE mediated by endophilin studied here, a scaffold of endophilin BAR domains imposes the frictional force on the membrane tube, mechanically connected to the neck, while the motor dynein provides the pulling force for tube extension, enabling FDS.

Scaffold slows lipid diffusion

Friction results from interactions between the protein scaffold and the lipid membrane. We found that the scaffold dramatically reduces the mobility of lipids underneath, with important consequences for sorting in nascent endocytic membrane carriers. Once a scaffold is formed on a pre-endocytic bud, diffusion of membrane-containing cargos on the bud back to the plasma membrane is impaired, which could thereby kinetically trap them. This effect may, however, be opposed by influx of new cargoes across the scaffold by advection due to tube elongation. Advection would occur on timescales greater than the characteristic time t^* set by the friction coefficient and the pulling speed (see Equation 4). As a case in point, micro-compartmentation of certain lipids is critical for auxilin recruitment to the clathrin-coated bud just before scission, enabling the uncoating of the fully formed clathrin-coated vesicle (Massol et al., 2006). This was suggested to be due to diffusion-limited accumulation of auxilin-binding lipids in the bud at the right time and place upon scaffolding by BAR-domain proteins.

Scission of spherical *vs.* tubular vesicles

A surprising finding of our work is that endoA2 forms a scaffold that stabilizes pre-formed membrane tubes, whereas the same protein spontaneously fragments small spherical vesicles (Boucrot et al., 2012). What is the origin of this apparent discrepancy? The initial morphology of the membrane could be crucial in determining whether the insertion leads to membrane scission or the stabilization of curvature. Earlier studies indicate that there is a fundamental difference in the way BAR proteins interact with spherical *vs*. cylindrical membranes (Ambroso et al., 2014). In fact, α-helices favor positive Gaussian membrane curvature, and are thus able to drive a topological transformation from a vesicle to several smaller ones (Boucrot et al., 2012). This effect depends on the depth of insertion: as the insertion gets closer to the bilayer middle plane, the effect becomes smaller (Campelo et al., 2008). On small spherical vesicles, the BAR domain backbone is not tightly bound to the membrane and the insertion is therefore shallow (Ambroso et al., 2014) favoring vesiculation. In contrast, on a pre-formed nanotube, the same proteins bind closely to the tube, forming a scaffold (Simunovic et al., 2016); AH inserts deeper (Ambroso et al., 2014), and there is no incentive to spontaneously undergo scission. This effect resolves the apparent discrepancy. The dueling effects of the insertion and the backbone can be illustrated by considering CME. In the late stage of CME in mammalian cells, the clathrin-coated spherical membrane bud is connected to the flat membrane by a short neck with negative Gaussian curvature. In this case, insertion of α-helices—from endophilin or from the ENTH domain of epsin—destabilizes the neck, favoring scission. The shape of the neck prevents its stabilization by the BAR backbone. In CIE or in our tube experiments, we expect that the backbone effect overwhelms the insertion one. However, in CME in yeast, which poorly relies on dynamin, the BAR domain of

Rvs161/167p (homologous to mammalian amphiphysin 1) stabilizes the neck into a long cylinder; here, scission could occur through FDS, generated by the pulling force of actin.

We therefore propose that depending on the presence of α-helices, BAR domain proteins function directly via two distinct mechanisms in scission. First, if the nascent bud is spherical, attached to the donor membrane (i.e. the plasma membrane for CME in mammalian cells, or endoplasmatic reticulum and Golgi for COPII or COPI-coated vesicles, respectively) by a short, curved neck then its shape is inherently destabilized by insertions (those of Sar1 for COPII, and of Arf1 for COPI). Second, if the bud is tubular, it is not vulnerable to scission via insertions, but might undergo FDS. In this case, donors are the plasma membrane (for endocytosis of toxins and growth factors such as EGF) and possibly also endosomes where sortin nexins provide scaffolding, and the elongation force comes from actin polymerization and/or motors, e.g. in (Traer et al., 2007). Furthermore, it seems likely that yeast CME, and mammalian CME at high membrane tensions, function in a hybrid manner; they combine a spherical bud with a long, stabilized neck, and require actin to undergo scission.

Role of the cytoskeleton

FDS is a generic scission module that hinges on a few basic elements, namely a protein scaffold and a tube extension force; see Figure 6 and Box 1. Our discovery that molecular motors walking on microtubules can pull quickly enough to break a membrane tube when associated with protein scaffolds opens exciting new routes for future investigations. Depending on the microtubule orientation—i.e., at the plasma membrane or at the Golgi apparatus—different motor families are expected to be involved in tube scission. Alternatively, the pulling force for FDS could be provided by actin polymerization (Figure 6). Actin has been shown to be involved widely in endocytosis (Mooren et al., 2012), in particular in CME in mammalian and yeast cells (Boulant et al., 2011; Ferguson et al., 2009; Grassart et al., 2014), and also in CIE (Renard et al., 2015).

Possible interplay with dynamin

FDS provides a scission mechanism in situations where dynamin is dispensable. Yet, both mechanisms can nevertheless coexist and be cumulative. In mammalian cells, CME generally involves dynamin for clathrin vesicle budding, although synergistic effects between N-BAR-domain proteins and dynamin on their mutual recruitment and dynamin GTPase activity have been reported (Meinecke et al., 2013; Neumann and Schmid, 2013; Sundborger et al., 2011; Taylor et al., 2012; Yoshida et al., 2004). In CIE, endophilin-mediated FDS acts in parallel with dynamin GTPase-induced scission (Renard et al., 2015), thereby building robustness into the process. We propose here that N-BAR-domain proteins can additionally assist dynamin-mediated scission a) by establishing a mechanical docking for the dynamin coat to the plasma membrane allowing FDS to occur for the dynamin-scaffolded neck if actin polymerization or motors provide extensional force, and b) by directly contributing to neck scission by FDS.

Fast endocytosis

Endophilin A1 and A2 are known to participate in fast endocytosis in neurons, occurring on a timescale of seconds (Boucrot et al., 2015; Llobet et al., 2011). Our experiments revealed that endophilin-dependent FDS, enabled by microtubule-based motors, occurs on the order of a few tens of seconds. This difference in timescales could be related to other scission modules

(dynamin, actin), which can act in parallel *in vivo* and make the scission process very fast altogether. It could also be due to the relatively higher proportion of polyunsaturated lipids in neuronal membranes (Yang et al., 2012), as compared with our experiments. The presence of these lipids could result in a decrease of the membrane bending rigidity, κ, and an increase in the number of lipid packing defects (Pinot et al., 2014). While the effect of a decrease in κ on the scission time is not expected to be very strong (SI), the effect of packing defects could be dramatic. These defects should facilitate AH insertion, thereby increasing the scaffold-membrane friction, which would decrease scission time (see equation 10). Perhaps more significantly, an increase in the degree of lipid chain unsaturation reduces the membrane edge tension, γ (Evans et al., 2003), which will lower the energy barrier for nucleating a membrane pore prior to scission. Since the barrier decreases exponentially with decreasing edge tension (see equation 6 and associated discussion), lipid unsaturation could lower the scission time by orders of magnitude, making FDS relevant to fast scission in neurons.

CONCLUSION

We have shown that in the presence of a pulling force, provided by motors or actin, BAR domain scaffolds enable scission through a generic friction-based mechanism. Whereas α-helices contribute to destabilizing (severing) spherical buds, they are not required for FDS of tubes. The timescales associated with FDS are highly variable and can be adjusted by varying the membrane lipid composition, tuning FDS for different cellular contexts. Since BAR domains are ubiquitous, FDS is a basic and versatile scission mechanism that could occur throughout the cell and across cell types. This mechanism could, in principle, be extended to any protein that binds to membrane tubes, in which the resulting assembly imposes sufficient friction. Finally, this work could open new avenues of study into the competing tendencies of N-BAR proteins to stabilize or effect scission of transport intermediates.

AUTHOR CONTRIBUTIONS

M.S., J.B.M., K.R., and D.B. performed and analyzed experiments. M.S. and P.B. conceived experiments. A.C.J. and J.P. conceived and developed the theory. P.B. secured funding. H.F.R., E.E. provided proteins. H.F.R., E.E., K.R., A.K., G.V., H.M.M. and L.J. provided conceptual advice and feedback. M.S., P.B., and A.C.-J. wrote the manuscript. All authors discussed the results and commented on the manuscript.

ACKNOWLEDGMENTS

We thank Laura Picas and Marta Bally for assistance in membrane sheet and supported bilayer experiments. M.S. and G.A.V. acknowledge the support of the National Institutes of Health (grant R01-GM063796), P.B. and L.J. of the Agence Nationale pour la Recherche (ANR-11BSV201403 to P.B. and ANR-16-CE23-0005-02 to L.J.), L.J. of the European Research Council advanced grant (project 340485), E.E. and H.T.M of the Medical Research Council UK (grant U105178795), A.K.K. of the National Institutes of Health (grant R01 GM106720). M.S. was funded in part by the Chateaubriand fellowship and the France and Chicago Collaborating in the Sciences grant, and received support from the University Paris Diderot. The P.B. group belongs to the CNRS consortium CellTiss, P.B., J.P. and L.J. groups to the Labex CelTisPhyBio (ANR-11-LABX0038), and to Paris Sciences et Lettres (ANR-10-IDEX-0001-02).

REFERENCES

Allain, J.M., Storm, C., Roux, A., Ben Amar, M., and Joanny, J.F. (2004). Fission of a multiphase membrane tube. Phys Rev Lett *93*, 158104.

Ambroso, M.R., Hegde, B.G., and Langen, R. (2014). Endophilin A1 induces different membrane shapes using a conformational switch that is regulated by phosphorylation. Proc Natl Acad Sci U S A *111*, 6982-6987.

Berk, D.A., Clark, A., Jr., and Hochmuth, R.M. (1992). Analysis of lateral diffusion from a spherical cell surface to a tubular projection. Biophys J *61*, 1-8.

Boucrot, E., Ferreira, A.P., Almeida-Souza, L., Debard, S., Vallis, Y., Howard, G., Bertot, L., Sauvonnet, N., and McMahon, H.T. (2015). Endophilin marks and controls a clathrin-independent endocytic pathway. Nature *517*, 460-465.

Boucrot, E., Pick, A., Camdere, G., Liska, N., Evergren, E., McMahon, H.T., and Kozlov, M.M. (2012). Membrane fission is promoted by insertion of amphipathic helices and is restricted by crescent BAR domains. Cell *149*, 124-136.

Boulant, S., Kural, C., Zeeh, J.C., Ubelmann, F., and Kirchhausen, T. (2011). Actin dynamics counteract membrane tension during clathrin-mediated endocytosis. Nat Cell Biol *13*, 1124-1131.

Brochard-Wyart, F., Borghi, N., Cuvelier, D., and Nassoy, P. (2006). Hydrodynamic narrowing of tubes extruded from cells. Proc Natl Acad Sci U S A *103*, 7660-7663.

Callan-Jones, A., Durand, M., and Fournier, J.-B. (2016). Hydrodynamics of bilayer membranes with diffusing transmembrane proteins. Soft matter.

Campelo, F., McMahon, H.T., and Kozlov, M.M. (2008). The hydrophobic insertion mechanism of membrane curvature generation by proteins. Biophys J *95*, 2325-2339.

Campillo, C., Sens, P., Koster, D., Pontani, L.L., Levy, D., Bassereau, P., Nassoy, P., and Sykes, C. (2013). Unexpected membrane dynamics unveiled by membrane nanotube extrusion. Biophys J *104*, 1248-1256.

Chen, Z., Zhu, C., Kuo, C.J., Robustelli, J., and Baumgart, T. (2016). The N-Terminal Amphipathic Helix of Endophilin Does Not Contribute to Its Molecular Curvature Generation Capacity. J Am Chem Soc *138*, 14616-14622.

Cuvelier, D., Derenyi, I., Bassereau, P., and Nassoy, P. (2005). Coalescence of membrane tethers: experiments, theory, and applications. Biophys J *88*, 2714-2726.
Day, C.A., Baetz, N.W., Copeland, C.A., Kraft, L.J., Han, B., Tiwari, A., Drake, K.R., De Luca, H., Chinnapen, D.J., Davidson, M.W., *et al.* (2015). Microtubule motors power plasma membrane tubulation in clathrin-independent endocytosis. Traffic *16*, 572-590.
Derenyi, I., Julicher, F., and Prost, J. (2002). Formation and interaction of membrane tubes. Phys Rev Lett *88*, 238101.
Domanov, Y.A., Aimon, S., Toombes, G.E., Renner, M., Quemeneur, F., Triller, A., Turner, M.S., and Bassereau, P. (2011). Mobility in geometrically confined membranes. Proc Natl Acad Sci U S A *108*, 12605-12610.
Dommersnes, P., Orwar, O., Brochard-Wyart, F., and Joanny, J. (2005). Marangoni transport in lipid nanotubes. EPL (Europhysics Letters) *70*, 271.
Evans, E., Heinrich, V., Ludwig, F., and Rawicz, W. (2003). Dynamic tension spectroscopy and strength of biomembranes. Biophys J *85*, 2342-2350.
Evans, E., and Yeung, A. (1994). Hidden Dynamics in Rapid Changes of Bilayer Shape. Chem Phys Lipids *73*, 39-56.
Ferguson, S.M., Raimondi, A., Paradise, S., Shen, H., Mesaki, K., Ferguson, A., Destaing, O., Ko, G., Takasaki, J., Cremona, O., *et al.* (2009). Coordinated actions of actin and BAR proteins upstream of dynamin at endocytic clathrin-coated pits. Dev Cell *17*, 811-822.
Garcia-Saez, A.J., Chiantia, S., Salgado, J., and Schwille, P. (2007). Pore formation by a Bax-derived peptide: effect on the line tension of the membrane probed by AFM. Biophys J *93*, 103-112.
Grassart, A., Cheng, A.T., Hong, S.H., Zhang, F., Zenzer, N., Feng, Y., Briner, D.M., Davis, G.D., Malkov, D., and Drubin, D.G. (2014). Actin and dynamin2 dynamics and interplay during clathrin-mediated endocytosis. J Cell Biol *205*, 721-735.
Hassinger, J.E., Oster, G., Drubin, D.G., and Rangamani, P. (2017). Design principles for robust vesiculation in clathrin-mediated endocytosis. Proc Natl Acad Sci U S A *114*, E1118-E1127.
Johannes, L., Parton, R.G., Bassereau, P., and Mayor, S. (2015). Building endocytic pits without clathrin. Nat Rev Mol Cell Biol *16*, 311-321.
Keller, J.B., and Rubinow, S.I. (1976). Slender-body theory for slow viscous flow. J Fluid Mech *75*, 705-714.
Kirchhausen, T., Owen, D., and Harrison, S.C. (2014). Molecular structure, function, and dynamics of clathrin-mediated membrane traffic. Cold Spring Harb Perspect Biol *6*, a016725.
Koster, G., VanDuijn, M., Hofs, B., and Dogterom, M. (2003). Membrane tube formation from giant vesicles by dynamic association of motor proteins. Proc Natl Acad Sci U S A *100*, 15583-15588.
Kozlovsky, Y., and Kozlov, M.M. (2003). Membrane fission: model for intermediate structures. Biophys J *85*, 85-96.
Kramers, H.A. (1940). Brownian motion in a field of force and the diffusion model of chemical reactions. Physica *7*, 284-304.
Kwok, R., and Evans, E. (1981). Thermoelasticity of large lecithin bilayer vesicles. Biophys J *35*, 637-652.
Landau, L., and Lifshitz, E. (1980). Statistical Physics, Part 1: Volume 5.
Leduc, C., Campas, O., Joanny, J.F., Prost, J., and Bassereau, P. (2010). Mechanism of membrane nanotube formation by molecular motors. Biochim Biophys Acta *1798*, 1418-1426.

Leduc, C., Campas, O., Zeldovich, K.B., Roux, A., Jolimaitre, P., Bourel-Bonnet, L., Goud, B., Joanny, J.F., Bassereau, P., and Prost, J. (2004). Cooperative extraction of membrane nanotubes by molecular motors. Proc Natl Acad Sci U S A *101*, 17096-17101.
Lee, M.T., Hung, W.C., Chen, F.Y., and Huang, H.W. (2008). Mechanism and kinetics of pore formation in membranes by water-soluble amphipathic peptides. Proc Natl Acad Sci U S A *105*, 5087-5092.
Liu, J., Kaksonen, M., Drubin, D.G., and Oster, G. (2006). Endocytic vesicle scission by lipid phase boundary forces. Proc Natl Acad Sci U S A *103*, 10277-10282.
Liu, J., Sun, Y., Drubin, D.G., and Oster, G.F. (2009). The mechanochemistry of endocytosis. PLoS Biol *7*, e1000204.
Llobet, A., Gallop, J.L., Burden, J.J., Camdere, G., Chandra, P., Vallis, Y., Hopkins, C.R., Lagnado, L., and McMahon, H.T. (2011). Endophilin drives the fast mode of vesicle retrieval in a ribbon synapse. J Neurosci *31*, 8512-8519.
Massol, R.H., Boll, W., Griffin, A.M., and Kirchhausen, T. (2006). A burst of auxilin recruitment determines the onset of clathrin-coated vesicle uncoating. Proc Natl Acad Sci U S A *103*, 10265-10270.
McMahon, H.T., and Boucrot, E. (2011). Molecular mechanism and physiological functions of clathrin-mediated endocytosis. Nat Rev Mol Cell Biol *12*, 517-533.
Meinecke, M., Boucrot, E., Camdere, G., Hon, W.C., Mittal, R., and McMahon, H.T. (2013). Cooperative recruitment of dynamin and BIN/amphiphysin/Rvs (BAR) domain-containing proteins leads to GTP-dependent membrane scission. J Biol Chem *288*, 6651-6661.
Merkel, R., Sackmann, E., and Evans, E. (1989). Molecular friction and epitactic coupling between monolayers in supported bilayers. Journal de Physique *50*, 1535-1555.
Merrifield, C.J., and Kaksonen, M. (2014). Endocytic accessory factors and regulation of clathrin-mediated endocytosis. Cold Spring Harb Perspect Biol *6*, a016733.
Montes, L.R., Alonso, A., Goni, F.M., and Bagatolli, L.A. (2007). Giant unilamellar vesicles electroformed from native membranes and organic lipid mixtures under physiological conditions. Biophys J *93*, 3548-3554.
Mooren, O.L., Galletta, B.J., and Cooper, J.A. (2012). Roles for actin assembly in endocytosis. Annu Rev Biochem *81*, 661-686.
Morlot, S., Galli, V., Klein, M., Chiaruttini, N., Manzi, J., Humbert, F., Dinis, L., Lenz, M., Cappello, G., and Roux, A. (2012). Membrane shape at the edge of the dynamin helix sets location and duration of the fission reaction. Cell *151*, 619-629.
Neumann, S., and Schmid, S.L. (2013). Dual role of BAR domain-containing proteins in regulating vesicle release catalyzed by the GTPase, dynamin-2. J Biol Chem *288*, 25119-25128.
Peter, B.J., Kent, H.M., Mills, I.G., Vallis, Y., Butler, P.J., Evans, P.R., and McMahon, H.T. (2004). BAR domains as sensors of membrane curvature: the amphiphysin BAR structure. Science *303*, 495-499.
Picas, L., Viaud, J., Schauer, K., Vanni, S., Hnia, K., Fraisier, V., Roux, A., Bassereau, P., Gaits-Iacovoni, F., Payrastre, B., *et al.* (2014). BIN1/M-Amphiphysin2 induces clustering of phosphoinositides to recruit its downstream partner dynamin. Nat Commun *5*, 5647.
Pinot, M., Vanni, S., Pagnotta, S., Lacas-Gervais, S., Payet, L.A., Ferreira, T., Gautier, R., Goud, B., Antonny, B., and Barelli, H. (2014). Lipid cell biology. Polyunsaturated phospholipids facilitate membrane deformation and fission by endocytic proteins. Science *345*, 693-697.
Rangamani, P., Mandadap, K.K., and Oster, G. (2014). Protein-induced membrane curvature alters local membrane tension. Biophys J *107*, 751-762.

Rawicz, W., Olbrich, K.C., McIntosh, T., Needham, D., and Evans, E. (2000). Effect of chain length and unsaturation on elasticity of lipid bilayers. Biophys J *79*, 328-339.
Renard, H.F., Simunovic, M., Lemiere, J., Boucrot, E., Garcia-Castillo, M.D., Arumugam, S., Chambon, V., Lamaze, C., Wunder, C., Kenworthy, A.K., *et al.* (2015). Endophilin-A2 functions in membrane scission in clathrin-independent endocytosis. Nature *517*, 493-496.
Romer, W., Pontani, L.L., Sorre, B., Rentero, C., Berland, L., Chambon, V., Lamaze, C., Bassereau, P., Sykes, C., Gaus, K., *et al.* (2010). Actin dynamics drive membrane reorganization and scission in clathrin-independent endocytosis. Cell *140*, 540-553.
Roux, A., Cappello, G., Cartaud, J., Prost, J., Goud, B., and Bassereau, P. (2002). A minimal system allowing tubulation with molecular motors pulling on giant liposomes. Proc Natl Acad Sci U S A *99*, 5394-5399.
Roux, A., Uyhazi, K., Frost, A., and De Camilli, P. (2006). GTP-dependent twisting of dynamin implicates constriction and tension in membrane fission. Nature *441*, 528-531.
Saarikangas, J., Zhao, H., Pykalainen, A., Laurinmaki, P., Mattila, P.K., Kinnunen, P.K., Butcher, S.J., and Lappalainen, P. (2009). Molecular mechanisms of membrane deformation by I-BAR domain proteins. Curr Biol *19*, 95-107.
Schmid, S.L., Sorkin, A., and Zerial, M. (2014). Endocytosis: Past, present, and future. Cold Spring Harb Perspect Biol *6*, a022509.
Sciaky, N., Presley, J., Smith, C., Zaal, K.J., Cole, N., Moreira, J.E., Terasaki, M., Siggia, E., and Lippincott-Schwartz, J. (1997). Golgi tubule traffic and the effects of brefeldin A visualized in living cells. J Cell Biol *139*, 1137-1155.
Shnyrova, A.V., Bashkirov, P.V., Akimov, S.A., Pucadyil, T.J., Zimmerberg, J., Schmid, S.L., and Frolov, V.A. (2013). Geometric catalysis of membrane fission driven by flexible dynamin rings. Science *339*, 1433-1436.
Simunovic, M., Evergren, E., Golushko, I., Prévost, C., Renard, H.F., Johannes, L., McMahon, H.T., Lorman, V., Voth, G.A., and Bassereau, P. (2016). How curvature-generating proteins build scaffolds on membrane nanotubes P Natl Acad Sci USA *In Press*.
Simunovic, M., Mim, C., Marlovits, T.C., Resch, G., Unger, V.M., and Voth, G.A. (2013). Protein-mediated transformation of lipid vesicles into tubular networks. Biophys J *105*, 711-719.
Skjeldal, F.M., Strunze, S., Bergeland, T., Walseng, E., Gregers, T.F., and Bakke, O. (2012). The fusion of early endosomes induces molecular-motor-driven tubule formation and fission. J Cell Sci *125*, 1910-1919.
Sorre, B., Callan-Jones, A., Manzi, J., Goud, B., Prost, J., Bassereau, P., and Roux, A. (2012). Nature of curvature coupling of amphiphysin with membranes depends on its bound density. Proc Natl Acad Sci U S A *109*, 173-178.
Soykan, T., Maritzen, T., and Haucke, V. (2016). Modes and mechanisms of synaptic vesicle recycling. Curr Opin Neurobiol *39*, 17-23.
Sundborger, A., Soderblom, C., Vorontsova, O., Evergren, E., Hinshaw, J.E., and Shupliakov, O. (2011). An endophilin-dynamin complex promotes budding of clathrin-coated vesicles during synaptic vesicle recycling. J Cell Sci *124*, 133-143.
Takei, K., Slepnev, V.I., Haucke, V., and De Camilli, P. (1999). Functional partnership between amphiphysin and dynamin in clathrin-mediated endocytosis. Nat Cell Biol *1*, 33-39.
Taylor, M.J., Lampe, M., and Merrifield, C.J. (2012). A feedback loop between dynamin and actin recruitment during clathrin-mediated endocytosis. PLoS Biol *10*, e1001302.
Traer, C.J., Rutherford, A.C., Palmer, K.J., Wassmer, T., Oakley, J., Attar, N., Carlton, J.G., Kremerskothen, J., Stephens, D.J., and Cullen, P.J. (2007). SNX4 coordinates endosomal

sorting of TfnR with dynein-mediated transport into the endocytic recycling compartment. Nat Cell Biol *9*, 1370-1380.
Walani, N., Torres, J., and Agrawal, A. (2015). Endocytic proteins drive vesicle growth via instability in high membrane tension environment. Proc Natl Acad Sci U S A *112*, E1423-1432.
Yang, H.J., Sugiura, Y., Ikegami, K., Konishi, Y., and Setou, M. (2012). Axonal gradient of arachidonic acid-containing phosphatidylcholine and its dependence on actin dynamics. J Biol Chem *287*, 5290-5300.
Yoshida, Y., Kinuta, M., Abe, T., Liang, S., Araki, K., Cremona, O., Di Paolo, G., Moriyama, Y., Yasuda, T., De Camilli, P., *et al.* (2004). The stimulatory action of amphiphysin on dynamin function is dependent on lipid bilayer curvature. EMBO J *23*, 3483-3491.

MAIN FIGURE TITLES AND LEGENDS

Figure 1. External pulling force induces scission of endophilin-scaffolded tubes.
A) Force, *f*, as a function of time, *t*, during the extension of a protein-scaffolded tube at speed *V*. For endoA2 WT, $V = 1.02$ μm.s^{-1}; for endoA2 ΔH0, $V = 1.15$ μm.s^{-1}; for endoA2 mut, $V = 0.95$ μm.s^{-1}; and for centaurin (centa), $V = 0.5$ μm.s^{-1}. Gray: control (no proteins), $V = 0.3$ μm.s^{-1} at vesicle tension $\sigma_v = 0.02$ mN.m^{-1}.
(B) A kymogram of scission by extending a tube partially scaffolded by endo A2 (corresponding to the endoA2 WT force data in A), demonstrating that the protein scaffold adjacent to the GUV moves as the GUV is pulled leftward by external force. Vertical axis is time; total time, 8.5 s. Arrows indicate the severed tube.
(C) Snapshots of scission by pulling an endoA2-scaffolded tube at 0.7 μm.s^{-1}, highlighting the presence of endoA2 on the GUV. Scale bar in all, 5 μm. See also Figures S1, S2, and S3 and Movies S1, S2, and S3.

Figure 2. Protein scaffold forms a lipid diffusion barrier.
(A) Confocal images after bleaching the bare (top left) and protein-scaffolded tube (top right). Bottom: fluorescence intensity recovery of lipids in the scaffolded tube ($I_{tub,rec}$) normalized by the pre-bleaching value ($I_{tub,ref}$) as a function of time (t) of photo recovery. Plot colors represent different independent experiments. Scale bar, 3 μm.
(B) Fluorescent image of a tube with coexisting scaffolded (thinner) and non-scaffolded (thicker) domains. Inset shows overlaid green (N-BAR domain) and red (lipid) channel. Graph shows the tube fluorescent intensity, normalized by the vesicle intensity, (I_{tub}/I_{ves}) on the non-scaffolded domain (black dots) and the calculation of what the tube radius would have been according to $r = \sqrt{\kappa/2\,\sigma_v}$ if tube tension were equilibrated (grey dots). During the experiment, σ_v was increased step-wise. The scaffold creates a diffusion barrier preventing a quick reduction in *r* of the un-scaffolded part. Scale bar, 3 μm.

Figure 3. Extending endophilin-coated tubes leads to force increase.
(A) Illustration of a protein-scaffolded tube extended at speed V. Relative motion between scaffold (green) and membrane tube (red) results in friction, with coefficient ξ, and an increase in the force, *f*.
(B) Force versus time for WT endophilin-coated tubes, pulled at a constant speed V, for ten different vesicles. Each data set is fitted with equation 3 for the given value V (as labeled, given in μm.s^{-1}). For clarity, the initial force, f_0 , has been subtracted. Inset: scission of a vesicle pulled at the lowest speed occurs on a longer time scale, and is shown separately.
(C) 3D plot of f vs. t and V, calculated from equation 3, shows increase of force with pulling speed, all other parameters remaining constant (f_0=2 pN, L_0 = 0.8 μm, ξ=30 Pa.s).
(D) Bar graph comparing the mean friction coefficient, ξ, for endoA2 WT, endoA2 ΔH0, and endo mut (error bars indicate s.e.m.). Average values are $\xi = 80 \pm 30$ Pa.s (endoA2 WT); $\xi = 39 \pm 19$ Pa.s (endoA2 ΔH0); and $\xi = 112 \pm 27$ Pa.s (endoA2 mut).
(E) Force after a sudden increase in tube length. Relaxation of the force occurs following two length jumps, ΔL_1=3 μm and $\Delta L_2 = 4$ μm.
(F) Fits to the force relaxation after the two steps (red boxed region in H) yield $\xi = 35 \pm 0.8$ Pa.s and $\xi \approx 73 \pm 2$ Pa.s (95% CL). The total bare length was estimated as $L = 4.95$ μm (obtained by integrating $\frac{d}{dt}\left(\frac{L}{f}\right) = 0$ across the step) after the first step, and $L = 8.6$ μm after the second one. The relaxation data were fitted numerically by solving equation 2. The

bending stiffness of the membrane was taken to be $\kappa = 45\ k_B T$ for all fits (Simunovic et al., 2016).
(G) Force versus time endoA2 ΔH0-coated tubes, pulled at constant speed (*N*=5). Inset: scission of a vesicle pulled at the lowest speed occurs on a longer time scale, and is shown separately.
(H) Force versus time endoA2 mut-coated tubes, pulled at constant speed (*N*=9).
(I) 3D plot of f vs. t and ξ, calculated from equation 3, shows increase of force with friction, all other parameters remaining constant (V = 2 μm.s^{-1}, f_0 = 4 pN L_0 = 0.8 μm). See also Figure S4.

Figure 4. Tube scission time and force as a function of pulling speed.
(A) Illustration of FDS via nucleation of a pore in the membrane at the scaffold/membrane edge. Opening a pore releases bending and stretching energy, while creation of an exposed edge costs energy per unit length, given by the line tension, γ. See also Figure S5 and Movie S3.
(B) Scission time data vs. pulling speed, V , for endoA2 WT. Data ($\log(t_{\mathrm{break}})$ vs $V^{2/3}$) suggest two speed regimes. Inset: numerical calculation of $\log(t_{\mathrm{break}})$ vs $V^{2/3}$ (round symbols), for f given by equation 5 (see SI). Asymptotic expressions for t_{break} (red line: $t_{\mathrm{break}} \gg t^*$; see equation 6. green line: $t_{\mathrm{break}} \ll t^*$; see equation S22) confirm that two pulling speed regimes exist. The crossover time $t^*(V^{2/3})$ is shown by a dashed line.
(C) Scission time data and fit at low V for endoA2 WT. A linear fit, using, equation 6, yields $\xi = 56 \pm 16$ Pa.s. Error reflects standard error in fit parameter obtained using nonlinear fitting method.
(D) Force supplied by tube extension until scission, Δf, vs. V. Data shown for endoA2 WT and mutants.
(E) Log-log plots of Δf vs. V at low V is consistent with theory prediction that $\Delta f \sim V^{1/3}$.
(F) Fits to Δf vs. $V^{1/3}$ at low V yields, using equation 5, $\xi = 30 \pm 12$ Pa.s (endoA2 WT); $\xi = 1.4 \pm 2$ Pa.s (endoA2 ΔH0); and $\xi = 66 \pm 6$ Pa.s (endoA2 mut). Error reflects standard error in fit parameter obtained using nonlinear fitting method.

Figure 5. Scission of tubes pulled by microtubule-associated motors.
(A) Time series showing the formation and motion of a cholera toxin B-subunit -containing tubular invagination in an ATP depleted COS-7 cell. Scale bar, 1 μm.
(B) Distribution of tube-tip velocities measured from a kymogram at each time segment (225 total segments) from a total of 25 tubes.
(C) Pulling a tube from a GUV by kinesin in the absence of other membrane-curving proteins. The onset of tube pulling is minutes after introducing ATP into the system. Fluorescence, lipids; scale bar, 2 μm.
(D) Time-lapse of two different experiments showing scission of endophilin-coated tubes mediated by kinesin. Arrows point to observed scission locations just prior to breakage. The second example shows two breakage events of a branched tube. Green, endophilin; red, lipids. Scale bars, 2 μm.
(E) Steady-state observations of membrane scission mediated by kinesin and endophilin. Shown are representative images of vesicles in the presence of kinesin and ATP without endophilin A2 (− endoA2) and in the presence of 2.5 μM endophilin A2 (+ endoA2). Fluorescence, lipids; scale bar, 20 μm. Plots show quantification of the frequency and morphological characteristics of tubes in the control (kinesin + ATP) and in the presence of

endophilin A2 (kinesin + ATP + endoA2). Observations taken after 30 min of reaction time. See also Figure S6 and Movies S4 and S5.

Figure 6. Schematics of endocytosis by FDS.
Hypothetic role of FDS *in vivo* enabled by BAR-domain scaffolding. In **a,** BAR domain proteins, such as endoA2, bind to the cytosolic leaflet of endocytic membrane invaginations, forming a scaffold. The membrane tube containing cargoes is extended by microtubule-based molecular motors, such as dyneins or kinesins. In **b**, tube elongation is aided by actin polymerization, up to the point where FDS occurs. In **c**, the BAR domain proteins, the motors, and actin disassemble from the endocytosed vesicle, which continues along the endocytic pathway.

MAIN TABLES AND LEGENDS

Table 1. Friction coefficients.
Scaffold-lipid friction coefficients for endoA2 WT and its mutants. See SI Theory for details on measurements and potential source of errors related to the measurement type. See also Figures 3 and 4.

SUPPLEMENTAL FIGURE TITLES AND LEGENDS

Figure S1. Membrane-curving proteins stabilize tensed and tensionless membrane tubes and do not cut them in the absence of external force. (A) Spontaneous tubulation of an aspired GUV injected with 1 μM endophilin A2 (monomer concentration in the pipette). Green, endophilin; red, lipids. (B) Spontaneous tubulation of a supported lipid bilayer by 1 μM endophilin A2 (monomer concentration in bulk). Fluorescence, lipids. (C) Spontaneous tubulation of GUVs by 1 μM β2 centaurin (monomer concentration in bulk). Green, centaurin; red, lipids. Scale bar (A-C), 5 μm. (D) Force, *f*, exerted by a membrane tube on a bead held in the optical trap (OT) at time *t* after the injection of 0.5–2.5 μM protein (left) and final confocal microscopy snapshots (right). Tested proteins: endophilin A2 (endo), β2 centaurin (centa). Fluorescence, lipids. Scale bar, 3 μm. (E) Differential interference contrast microscopy time-lapse images of multilamellar bilayer sheets incubated with 5 μM full length endophilin A2 (monomeric concentration). No change in tubule length or their amount observed in 30 min of imaging time. Membrane composition in (A), (C), (D), and (E): total brain extract + 5% PI(4,5)P2 (mol/mol), composition in (B): 30% DOPS, 70% DOPC. Scale bar, 5 μm. Related to Figure 1.

Figure S2. Elongating bare tubes does not induce scission. (A) Tube pulling force, *f*, as a function of time, *t*, upon elongation of a tube at a rate of 0.3 $\mu m.s^{-1}$, at different GUV tensions, σ_v. (B) A control example with faster elongation: 1.3 $\mu m.s^{-1}$ at 0.08 $mN.m^{-1}$. (C) Aggressive elongation pulses at ~20 $\mu m.s^{-1}$ at 0.08 $mN.m^{-1}$, where the vesicle was repeatedly brought back-and-forth. The force fluctuates due to pulses, as the lipids cannot equilibrate so fast, but rapidly equilibrates when ceasing to pull. The tube did not break after 12 pulses. Time stamp in fluorescent images corresponds to the time in the plot above. Scale bar, 10 μm. Related to Figure 1.

Figure S3. Very slow elongation does not induce scission. Pulling an endo-A2-scaffolded tube at 20 nm.s^{-1}. Related to Figure 1.

Figure S4. Measuring scaffolded tube radius, *r*, versus time, *t*, during extension leading to FDS. Note, due to high frequency imaging, some bleaching is observed. Different colors represent independent experiments at different pulling speeds: 5.1 μm.s^{-1} (purple), 0.17 μm.s^{-1} (orange), 0.33 μm.s^{-1} (green). Related to Figure 1.

Figure S5. Scaffold break-up upon elongation of a fully covered tube. Kymogram of a tube fully covered by a scaffold of N-BAR domain of endo A2, showing that the scaffold breaks apart upon elongation. This implies that fully and partially scaffolded tubes are equivalent, as far as FDS is concerned. Arrows point to scaffold breaks observable by our microscope. Scale bar, 2 μm. Related to Figure 3.

Figure S6. Molecular motors work with endo A2 to induce FDS. (A) Effect of dynein motor on STxB tubules. Incubation of HeLa cells for 1 h at 37 °C with **(i),** untreated (control) **(ii)** 50 μM dyngo-4a (dynamin inhibitor) and **(iii)** 50 μM dyngo-4a +100 μM ciliobrevin-D (dynein inhibitor), followed by incubation with STxB-A488 (5 μg ml^{-1}) for 10 min. Determination of tube length on fixed cells; ***P < 0.001 (One-way Anova test). Blue: Hoechst dye; green: STxB-A488. Data are mean ± SEM of two independent experiments (n = 25 cells per condition). (B) Left: kymogram of a CTxB-containing tube elongated by dynein in an ATP depleted COS-7 cell. The position of the line used to generate the kymogram is highlighted in orange in Figure 5A in the Main Text. Cholera toxin B-subunit is fluorescently labeled. Right: the corresponding trajectory of the tubule tip as a function of time as traced from the kymogram. (C) Left: traces of tip displacement over time for 25 different tubules. Each individual tubule is indicated by a different symbol. Right: the cumulative probability plot of the resulting 228 measurements of segment velocity calculated as the slope of the lines between individual data points. Note, the corresponding histogram is in Figure 5A in the Main Text. (D) Left: kymogram of a tubule extruded from a GUV by kinesin motors (split into six lines, with each line indicating the time of the first image), showing the growth of the tubule shown in Figure 5C in the Main Text. The total vertical length in each segment is 3.55 μm. Right: another example with many extruded tubules, taken one day following the experiment. The chamber was sealed with putty sealant and kept in the fridge overnight. Lipids are fluorescent. Scale bar, 2 μm. (E) Time-lapse microscopy of FDS of endo-A2-covered tubules pulled by kinesin motors. The arrow points to a scission location just prior to breakage. Overlaid fluorescence of lipids (red) and endo A2 (green). Scale bar, 2 μm. Related to Figure 5.

SUPPLEMENTAL MOVIE LEGENDS

Movie S1. Endo A2 N-BAR domain does not induce scission of tubular membranes. Confocal fluorescence time-lapse during injection of an N-BAR domain of endo A2 near a tube pulled from a micropipette-aspired GUV. Movie shows spontaneous tubulation of the GUV and the formation of a scaffold on the tube (causing it to buckle). No scission is observed under these conditions. Red, lipids; green, N-BAR domain. Related to Figure S1.

Movie S2. FDS of a tube partially scaffolded by endo A2. Movie shows extension of a tube partially scaffolded by endoA2 N-BAR domain leading up to scission at the tube- GUV interface. Shown are the confocal fluorescence time lapse (left) and the tube retraction force, *f*, both changing with time, *t*. Top left: N-BAR (green); center left: lipids (red); bottom left: overlay. Related to Figure 1.

Movie S3. FDS of a tube fully scaffolded by endo A2. Movie shows extension of a tube initially fully scaffolded by endoA2 N-BAR domain leading up to scission. After initial extension, gaps form in the scaffold making fully and partially scaffolded tubes equivalent in FDS. Shown are confocal fluorescence time lapse (left) and tube retraction force, *f*, both changing with time, *t*. Top left: N-BAR (green); center left: lipids (red); bottom left: overlay. Related to Figure 1.

Movie S4. FDS by kinesin. Confocal fluorescence time lapse showing two scission events of kinesin-pulled tubes connected to a GUV seconds after endo A2 injection into the system. Scale bar, 2 μm. Related to Figure 5 and Figure S6.

Movie S5. FDS by kinesin. Confocal fluorescence time lapse showing a scission event of a kinesin-pulled tube connected to a GUV seconds after endo A2 injection into the system. Shown is a different example from Movie S4. Scale bar, 2 μm. Related to Figure 5 and Figure S6.

STAR Methods

KEY RESOURCES TABLE

REAGENT or RESOURCE	SOURCE	IDENTIFIER
Chemicals, Peptides, and Recombinant Proteins		
Total brain extract lipids	Avanti Polar Lipids	cat# 131101P
L-α-phosphatidylinositol-4,5-bisphosphate (PI(4,5)P_2,)	Avanti Polar Lipids	cat# 840046P
1,2-Dioleoyl-sn-glycero-3-phosphatidylcholine (DOPC)	Avanti Polar Lipids	cat# 850375
1,2-dioleoyl-sn-glycero-3-phosphatidylserine (DOPS)	Avanti Polar Lipids	cat# 840035
1,2-distearoyl-sn-glycero-3-phosphoethanolamine-N-[biotinyl(polyethylene glycol)-2000] (DSPE-PEG(2000)-biotin)	Avanti Polar Lipids	cat# 880129
1,2-dioleoyl-sn-glycero-3-phospho-L-serine-N-(7-nitro-2-1,3-benzoxadiazol-4-yl) (NBD-PS)	Avanti Polar Lipids	cat# 810198C
1,2-dioleoyl-sn-glycero-3-phospho-L-serine-N-(7-nitro-2-1,3-benzoxadiazol-4-yl)	Avanti Polar Lipids	cat# 810198
BODIPY-TR-C5-ceramide	Molecular Probes	cat# D7540
endophilin A2 N-BAR domain	McMahon lab (see STAR Methods)	N/A
β2 centaurin	McMahon lab (see STAR Methods)	N/A
endophilin A2 ΔH0	Johannes lab (see STAR Methods)	N/A
endophilin A2 E37K, D41K	McMahon lab (see STAR Methods)	N/A
full length endophilin A2	Anne Schmidt lab	N/A
pGEX4T2	GE Healthcare	N/A
pGEX6P2	GE Healthcare	N/A
isopropyl β-D-1-thiogalactopyranoside	Sigma	cat# I5502
glutathione sepharose	GE Healthcare	cat# 17075601
thrombin	Serva	cat# 36402
S75 Sephadex	GE Healthcare	N/A
Alexa Fluor® 488 C5 Maleimide	Life Technologies	cat# A10254
Strep-Tactin column	IBA	N/A
QHP column	GE Healthcare	N/A
streptavidin-coated polystyrene beads 3 µm	Spherotech	cat# SVP-30-5
β-casein from bovine milk (>98%)	Sigma	cat# C6905
tubulin	Manneville lab	N/A
biotinylated kinesin	Manneville lab	N/A
Taxol (paclitaxel)	Sigma	N/A
imidazole	Sigma	I5513
ATP	Sigma	A1852
Dyngo-4a	Abcam	cat# AB120689
Ciliobrevin-D	Calbiochem	cat# 250401
Shiga toxin B-Subunit coupled to Alexa-A88 dye	Johannes lab	N/A
Hoechst 34580	Sigma Aldrich	cat# 63493
Alexa488-CTxB	Invitrogen	cat# C34775
2-deoxyglucose	Sigma Aldrich	cat# D8375
Sodium Azide	Sigma Aldrich	cat# S2002
HEPES	Mediatech	cat# 25-060-CI
BSA	Sigma Aldrich	A8806
Dulbecco's modified Eagle medium (DMEM)	Life Technologies	
Fetal bovine serum	Life Technologies	

Paraformaldehyde	Electron microscopy sciences	cat# 15710
Experimental Models: Cell Lines		
COS-7	ATCC	ATCC® CRL-1651™
HeLa C2TA	Johannes lab	N/A
Software and Algorithms		
Matlab	The Mathworks, Inc.	
Fiji	https://fiji.sc/	
Mathematica	Wolfram, Inc.	

Contact for Reagent and Resource Sharing

Further information and requests for resources and reagents should be directed to and will be fulfilled by the Lead Contact, Patricia Bassereau (pbassereau@curie.fr) while questions about the details of the theoretical model should be addressed to Andrew Callan-Jones (andrew.callan-jones@univ-paris-diderot.fr).

Experimental Models and Subject Details

Cell lines

HeLa C2TA cells were cultured in DMEM complete media supplemented with 10% Fetal Bovine Serum (FBS) + Pen-Strep antibiotics mixture (1x). The cells were cultured at 37 °C in 5% CO_2.

COS-7 cells were grown in Dulbecco's modified Eagle medium (DMEM) containing 10% fetal bovine serum at 37°C and 5% CO_2. Cells were plated in Matek glass bottom culture plates 2 days prior to the experiments.

In vitro reconstituted membranes

Lipids used to reconstitute the cell membrane *in vitro* were purchased (see Key Resources Table) and stored at −80 °C or aliquoted in $CHCl_3$ and kept at −20 °C. Once vesicles were prepared (see below), they were kept on ice and used within 3 h.

Method Details

Protein purification

Proteins used in this study were expressed and purified as part of our recent publication (Simunovic et al., 2016). We repeat the protocol here for completeness. Rat endophilin A2 WT (amino acids 1–247) and its mutant (E37K, D41K) were cloned into pGEX4T2. Mutations were made to create a clone with a single cysteine residue available for fluorescence labeling, to ensure the label does not interfere with membrane binding (C96A, C147A, and Q228C). Human β2 centaurin (amino acids 1–384) was cloned in pGEX6P2, mutating all cysteines (C10A, C42A, C53A, C156A, C321A, C316A, C329A, and C339A) and adding a new cysteine at the N terminus. GST-tagged proteins were expressed in BL21 DE3 bacteria at 18 °C overnight after induction by 150 mM isopropyl β-D-1-thiogalactopyranoside, lysed in buffer (50 mM HEPES at pH = 7.4, 500 mM NaCl, 2 mM DTT, and protease inhibitor mixture) under high pressure (high pressure homogenizer; Constant Systems). The cleared lysate was incubated with glutathione sepharose for 30 min at

4 °C. The GST tag was cleaved off using thrombin or PreScission protease and the cleaved protein was passed over a Q Sepharose anion exchange column followed by a gel filtration column (S75 Sephadex). Endophilin A2 N-BAR domain and β2 centaurin were labeled with Alexa488 following the manufacturer's protocol (A10254), concentrated, snap-frozen in liquid nitrogen, and stored at −80 °C.

C-terminally strep-tagged mouse endoA2 ΔH0 was expressed in bacteria and purified on Strep-Tactin column as previously described (Renard et al., 2015). Eluates were loaded on a QHP column and eluted with a linear NaCl gradient in buffer (100 mM Tris-HCl at pH = 8.0, 1 mM EDTA). Fractions containing endoA2-Strep were then pooled and loaded on a Superdex 200 column for size exclusion chromatography. Protein purity was validated by SDS-polyacrylamide gel electrophoresis then endoA2 ΔH0-containing fractions were snap frozen in liquid nitrogen and stored at −80 °C.

The full-length mouse endophilin A2 (N-BAR + SH3 domains) was a generous gift of Anne Schmidt, Institut Jacques Monod, Université Paris Diderot.

Preparation of giant unilamellar vesicles (GUVs)

GUVs were prepared by electroformation on Pt-wires under quasi-physiological salt conditions (Montes et al., 2007). First, we mixed $CHCl_3$-solutions of the total brain extract and $PI(4,5)P_2$ at 95:5 (molar ratio, molar mass of brain extract estimated to be 800 $g.mol^{-1}$) to which we added 1% BODIPY-TR-C5-ceramide and ~0.1% DSPE-PEG(2000)-biotin (both molar percent). The lipid mix was applied to a pair of Pt-wires, in drops separated by 0.5 cm (total ~4 μL). The wires were dried under vacuum for 30–60 min then hydrated in a solution of 70 mM NaCl, 100 mM sucrose, and 10 mM tris, at pH = 7.4. We then applied AC current through the Pt-wires (assembled into a homemade Teflon chamber), using a functional generator, at 500 Hz and 280 mV overnight in the fridge. We disconnected the wires just prior to each experiment and used vesicles for no more than 4 h. We collected vesicles directly from the wires using a pipette (~10 μL of final solution per droplet of the lipid mix).

Preparation of supported bilayers

To make a supported lipid bilayer used in Figure 1, first the lipid mix composed of DOPC:DOPS (7:3, molar ratio) with 0.5% NBD-PS (molar percent), was dried under nitrogen to obtain 1 mg of dry mass. The mix was hydrated in 1 mL sucrose then extruded through a 100 nm polycarbonate filter. Thus-formed small vesicles were deposited onto an acid-cleaned coverslip to create a supported bilayer. The bilayer was rinsed with a solution of 100 mM NaCl and 10 mM tris buffer (pH = 7.4) and observed before and after adding the protein to a total bulk concentration of 3 μM using Nikon eclipse Ti inverted microscope.

Preparation of tensionless multilamellar lipid sheets

Multilamellar lipid sheets were prepared first by depositing a drop of the above-prepared brain extract–$PI(4,5)P_2$ lipid mix onto an acid-cleaned glass slide. The deposit was dried for an hour under vacuum then rapidly hydrated with a solution of 100 mM NaCl and 10 mM tris buffer (pH = 7.4). This process creates multilamellar sheets with many tensionless tubules emanating from the edges. We imaged the edges of the sheet with differential interference contrast microscopy before and after adding the protein (to a bulk concentration of 3 μM) for up to 30 min.

Pulling tubes from GUVs

The experiment was carried out very similarly as described previously (Sorre et al., 2012). First, the tip of the aspiration pipette (~5 μm in diameter at the tip) and the experimental chamber were immersed in a 5 $g.L^{-1}$ solution of β-casein (dissolved in 100 mM NaCl, 10 mM tris, pH = 7.4) for 30 min to minimize the adhesion of lipids to the glass surface. The chamber was then rinsed several times and filled with the experimental solution (100 mM NaCl and 40 mM glucose, 10 mM tris, pH = 7.4). The ionic strength of solutions used to grow GUVs and for tubule-extrusion experiments was confirmed to be within 10 mOsm using an osmometer (Loser, Germany) to avoid osmotic shock. While theoretically the solutions inside and outside the vesicle can be varied (keeping their ionic strengths equal), the composition we used seemed optimal for tube-pulling experiments. We caution the reader not to exceed 40 mM in glucose concentration as we found it inhibits streptavidin-biotin interactions.

GUVs were directly collected from Pt-wires just prior to the experiment and a few μL of the GUV solution was added to the experimental chamber. A few μL of streptavidin-coated polystyrene beads 3 μm in diameter were added to the experimental chamber as well to a final bead concentration around 0.1x10−3 % (w/v) or less.

Another pipette was filled with a solution of the protein (diluted in the experimental buffer to 1–5 μM monomeric concentration for all proteins except endoA2 ΔH0 where we used 7 μM monomeric concentration). The vesicles were left to deflate for 10–20 min after which we sealed the chamber with oil to prevent evaporation.

Vesicles with enough excess area to form an aspiration tongue were aspired in a micropipette, whose aspiration pressure sets membrane tension (Cuvelier et al., 2005; Kwok and Evans, 1981). By using a piezoactuator, we tethered the vesicle to a streptavidin-coated polystyrene bead trapped with optical tweezers, and gently pulled back, forming a tube between the vesicle and the bead. We observed the vesicle and the tube using confocal microscopy.

Fluorescence recovery after photobleaching (FRAP)

In the experiment, the lipid fluorophores in the ~10-μm-long tube were bleached by imaging only the tube region at full laser power (~ten images at a rate of 3 Hz; note that more than ten images runs the risk of photooxidation). Immediately after bleaching, the laser power was decreased and the system (vesicle + tube) imaged.

FDS by tube extension

We injected the protein near the tube at low pressure to avoid disturbing the system as descried previously (Sorre et al., 2012). After confirming the formation of a scaffold (force decrease and tube constriction, see Main text and (Simunovic et al., 2016)), we removed the injection pipette then applied a pulling force on the aspiration pipette, moving it away from the bead at a constant rate (50–8000 $nm.s^{-1}$). We determined the average pulling rate from time-lapse confocal images.

FDS by kinesin motors *in vitro*

We followed a previously described protocol for the extrusion of tubules from GUVs (Leduc et al., 2010; Leduc et al., 2004). *Polymerization of microtubules.* 50 μL of tubulin (at ~10 μM) was polymerized by incubation at 37°C for 15 min. We then added 2 μL of 1 mM taxol (diluted in water), which stabilizes the microtubules. We centrifuged the mix for 15 min at 37 °C, at 70 000 rpm (ultracentrifuge, rotor TLA-100). We removed the supernatant and re-suspended the sediment in 50 μL BRB (25 μL of 4X BRB, 75 μL H_2O, 3 μL of 1 mM taxol). We let the microtubules incubate for at least one day and we used them no more than 3 days

after preparation. *Coupling kinesin to microtubules.* We assembled an experimental chambers using a glass slide and a coverslip, attached by melting a strip of parafilm, with a total volume between the slides of ~5 μL. We filled the chamber with 5 μL polymerized microtubules and kept for 15 min at room temperature. Then, we incubated 5–10 μL of biotinylated kinesin (~10 μM) with 5 μL streptavidin (at comparable concentration as kinesin) for 15 min on ice. During incubation, we first rinsed the experimental chamber (containing microtubules) with ~10 μL of buffer composed of 97 μL of 50 mM imidazole (dissolved in 7 $g.L^{-1}$ casein) and 3 μL of 1 mM taxol, buffered to pH ~7. Importantly, the rinsing was done as carefully as possible, as fluxes in the chamber cause the polymerized microtubules to desorb from the glass. We incubated for 5 min at room temperature. Next, we rinsed (very carefully) with ~10 μL of buffer composed of 96.5 μL of 50 mM imidazole, 0.5 μL of 1 M DTT, and 3 μL of 1 mM taxol, buffered to pH ~7. We incubated for another 5 min. Finally, we injected the chamber with 5 μL kinesin that has been incubating with streptavidin. We incubated for at least 10 min. Note, this incubation step can be prolonged for a couple of hours if desired. *Kinesin-driven tube pulling.* To initiate the motors, we rinse the chamber with 10–15 μL motility buffer, composed of 89 μL experimental buffer (in our case, 40 mM glucose, 100 mM NaCl, and 10 mM tris, at pH = 7.4), 0.5 μL of 1 M DTT, 3 μL of 1 mM taxol, 2 μL of 100 mM ATP (freshly prepared), 3 μL of 4X oxygen scavenger (freshly prepared). In case the experimental buffer does not contain glucose, it needs to be added to the mix (2.5 μL of 1 M solution). Immediately after rinsing, 1–2 μL of highly concentrated solution of GUVs (prepared as described above) is added to the experimental chamber. After introducing GUVs, we tilt the chamber at 45° for one minute to help sediment the vesicles then mount it on the objective. We imaged as soon as possible. Note, that excessive exposure to fluorescent excitation can abort the motors due to oxidation.

FDS by dynein motors *in vivo*

To study the involvement of motor proteins that supply force needed to drive scission of STxB tubules, we inhibited the activity of dynein motors using Ciliobrevin-D (100 μM, 30 min, 37°C). Dynein motors can interact with plasma membrane tubules induced by STxB and drive the tubule extension by pulling the membrane along existing microtubules (Day et al., 2015). To test the involvement of dynein in STxB tubule elongation dynamics, we first inhibited the dynamin activity using Dyngo-4a (25 μM, 30 min, 37°C). In the presence of Dyngo-4a, STxB was localized in visible, micron-long tubular structures originating from plasma membrane (Fig. S6A, panels ii, iv). Further, upon inhibition of dynein in dynamin-inhibited cells, the tubule lengths decreased almost back to those under control condition (Fig S6A, panels iii, iv), indicating the strong involvement of the dynein motor in pulling the STxB tubules to provide force for scission.

Quantification and Statistical Analysis

Measuring membrane tension and force

The aspiration pressure in the pipette sets the membrane tension. At each tension step, the aspiration pressure is calculated from the hydrostatic pressure according to $\Delta P = \rho g h$, where ρ is the water density, g gravitational acceleration, and h the height of the water tank. Vesicle membrane tension, σ_{v}, is calculated using the Laplace equation: $\sigma_{\mathrm{v}} = \Delta P \frac{r_{\mathrm{pip}}}{2(1-r_{\mathrm{pip}}/r_{\mathrm{GUV}})}$ where r_{pip} and r_{GUV} are the radius of the pipette and the GUV, respectively. At the same time, equilibrium membrane force (tube-retraction force) is calculated from the Hooke law: $F = k(a - a_0)$ where a is the average position of the bead during that measurement and a_0 is the average position of the bead in the optical trap before pulling a tube. Both a and a_0 are

measured using videomicroscopy in bright field, while k is the stiffness of the optical trap (Sorre et al., 2012).

Measuring fluorescence intensity and tube radius

Fluorescence intensity of the membrane was taken by first fitting a line or a semicircle to, respectively, the maximum intensity segment of the tube or the GUV in confocal images (taken at the GUV equator), then calculating the mean intensity value along the fitted segment. Tube radius, r, can be measured from force and tension measurements (in the case of protein-free tubes) and from fluorescence (either protein-free or bound tubes). In Figure 2, r is measured as $r = \sqrt{\kappa/2\sigma_{\mathrm{v}}}$ (Derenyi et al., 2002). In Figure S4, r at each step is measured as $r = 10$ nm $I_{\mathrm{tub,curr}}/I_{\mathrm{tub,0}}$, where $I_{\mathrm{tub,curr}}/I_{\mathrm{tub,0}}$ is the lipid fluorescence intensity ratio in the tube between the current and the initial time steps, while the prefactor 10 nm is the initial endoA2 scaffold radius, determined previously (Simunovic et al., 2016).

Measuring scaffold friction coefficient

The friction coefficient between the protein scaffold and membrane tube was determined in four separate ways. First, the pulling force versus time data for single experiments on endoA2 WT, endoA2 mut, and endoA2 ΔH0 were fitted with equation 3 using the NonlinearModelFit function in Mathematica 11.0 (Figs. 4B, 4G, and 4H). The error on the extracted fitting parameters represents the standard error; the scale of variance was determined using the dispersion of the data (i.e., from a weighted sum of squares). The results of these fits for multiple experiments on endoA2 WT (N=10), endoA2 mut (N=9), and endoA2 ΔH0 (N=5) were compiled into a bar chart, in which the average values of the friction coefficient, ξ, are shown (Fig. 4D); the error bars represent the SEM.

The second method to find ξ was to fit the force versus time data for endoA2 mut-covered tubes subject to a sudden change in tube length (Figs. 4E and 4F). These data were fitted using equation S25, as described in the previous paragraph.

Next, the friction coefficient for endoA2 WT was also found from the scission times, t_{break}, as a function of pulling speed. These data, represented on log-lin scale, were fitted with equation 6 using the LinearModelFit function in Mathematica, as described above; see Fig. 5C. Finally, ξ was also obtained from the tube force at scission (minus the force before extension began), Δf, as a function of pulling speed. These data sets, for endoA2 WT, endoA2 mut, and endoA2 ΔH0, were fitted using equation 5 (Fig. 5F); a log-log representation of these data also allowed a fit of the exponent in the relation $\Delta f \propto V^{\alpha}$, for which our model predicts $\alpha = 1/3$.

Quantifying tube breakage in FDS

Tube breakage *in vitro* was readily visible from confocal time-lapse images (e.g, Figure 1C). Alternatively, a sudden drop in membrane force to zero marks FDS. In observations of tube stabilization (under static conditions) or tube scission (upon tube extension), N values, as indicated in Main text, represent the total number of pulled tubes, where no more than one tube was pulled from a GUV.

Fluorescence intensity of the membrane in the tube/GUV system was taken by fitting a line or a semicircle to, respectively, the tube or the GUV in the confocal image (taken at the GUV equator) then taking the average along the maximally intense line/curve. Average tube radius of an endophilin A2-scaffolded tube was previously measured to be 10 nm (Simunovic et al., 2016), which was taken as the initial value in Figure S4. The tube radius was calculated as

$R = 10\ \text{nm}\, I_{\text{tub,curr}}/I_{\text{tub,0}}$, where $I_{\text{tub,curr}}/I_{\text{tub,0}}$ is the ratio of the current and the lipid fluorescence intensity at the start of measurement (initiation of tube extension).

Cholera Toxin B tubulation assays were performed under ATP depleting conditions as previously described (Day et al., 2015). The cells were initially incubated in glucose-free DMEM containing 50 mM 2-deoxy-d-glucose, 0.02% sodium azide, 25 mM HEPES, and 1 mg/mL BSA for 15 min at 37 °C and 5% CO_2. They were rinsed twice and incubated for 5 min at room temperature with 100 nM Alexa 555 labeled CTxB. Subsequently, the cells were washed twice and imaged at 37 °C in the ATP depleted media. Under these conditions, CTxB tubules typically remain attached to the plasma membrane but on average increase in length over time. We also observed that some tubules undergo complex motions including bidirectional motility.

Kymographs were generated for individual tubules using the Multiple Kymograph plugin of ImageJ (Fiji). The movement of the leading edge of each tubule was used as the marker of the position of the tubule. This was manually tracked as a function of time in each of the kymographs. The tubule trajectories were then divided into segments based on directionality for velocity analysis. A change in direction was defined as a point at which the slope of the trajectories change and each slope represents a single instantaneous velocity of the tubule (25 tubules from 6 separate movies were chosen for analysis of tubule velocities and 228 instantaneous velocities were measured).

Quantification of STxB-induced tubule length under various experimental conditions (shown in Figure S6A) was done as previously described in (Renard et al., 2015). Tube recognition was done using a Fiji macro, which enhanced the tubular structures by computing eigenvalues of the Hessian matrix on Gaussian-filtered images (with sigma = 1 pixel), as implemented in the tubeness plugin. The threshold for tubules was done such that structures containing less than three pixels were discarded. If necessary, a manual correction of segmented tubules was performed upon a visual check. The tube-segmented structures were then reduced to a one-pixel-thick skeleton, using the Fiji plugin skeletonize. The pixel length of skeletonized tubules was then converted to actual length. In Figure S6A: ***P < 0.001 (One-way Anova test). Data are mean ± SEM of two independent experiments (N = 25 cells per condition).

Table 1

Measurement type	ξ_{WT} **(Pa.s)**	$\xi_{\Delta H0}$ **(Pa.s)**	ξ_{mut} **(Pa.s)**
Force *vs.* time	80±30	39±19	112±27
Breaking forces	30±12	1.4±2	66±6
Breaking times	56±16	—	—

Figure 1

Click here to download Figure Figure1.pdf

A

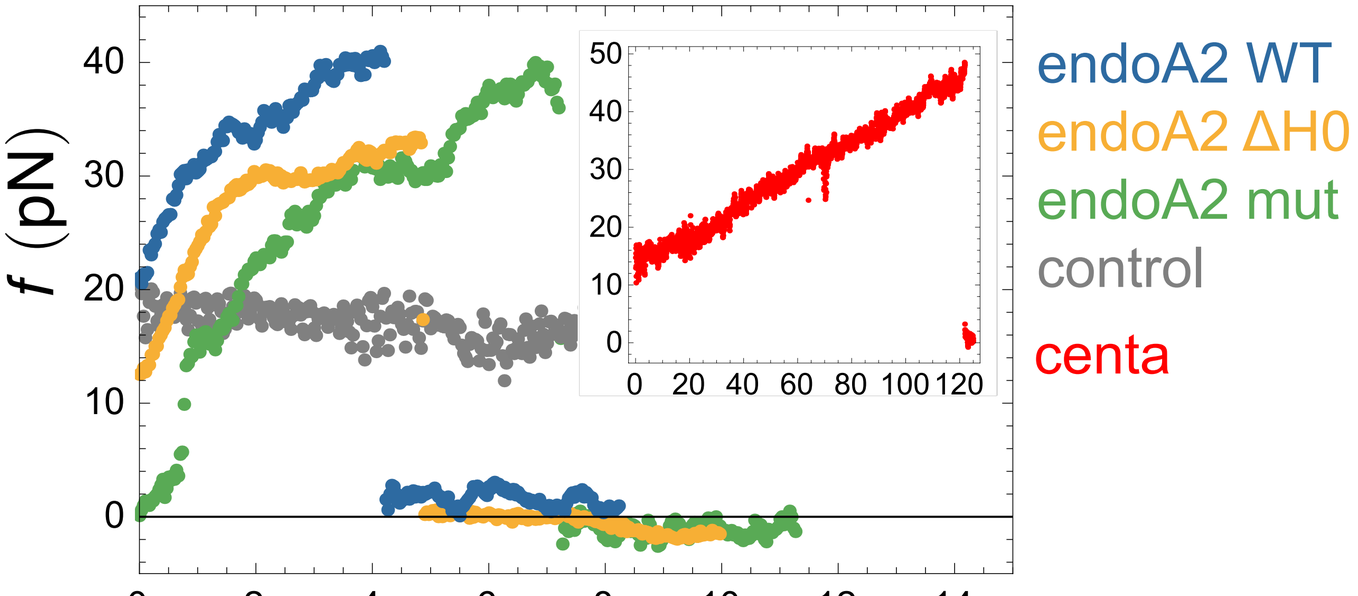

endoA2 WT
endoA2 ΔH0
endoA2 mut
control

centa

B

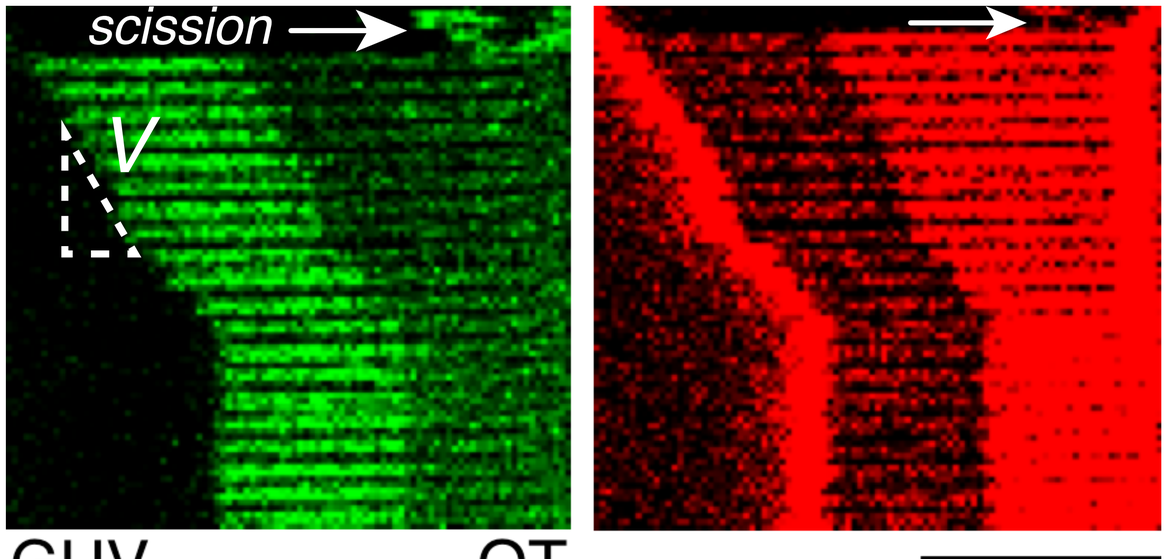

C

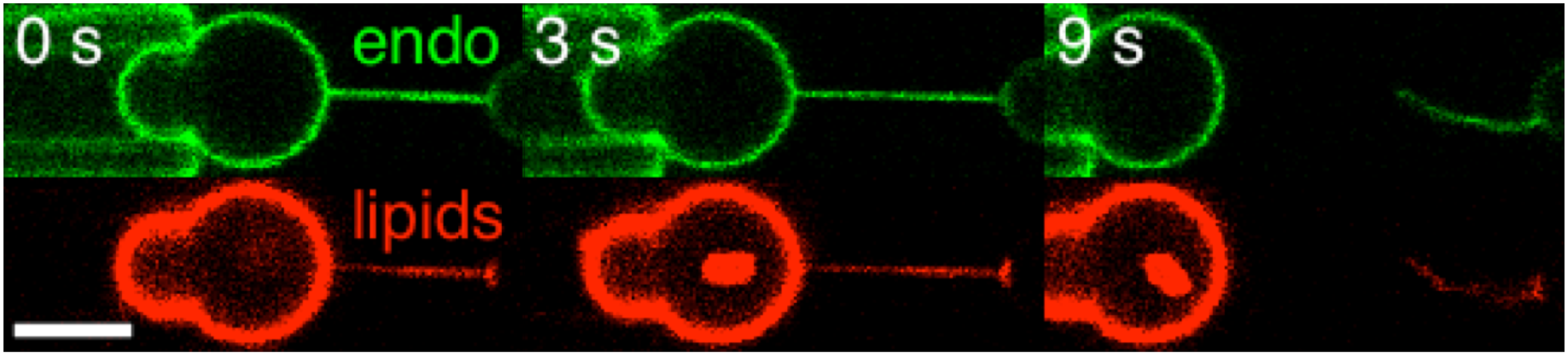

Figure 2

Click here to download Figure Figure2.png

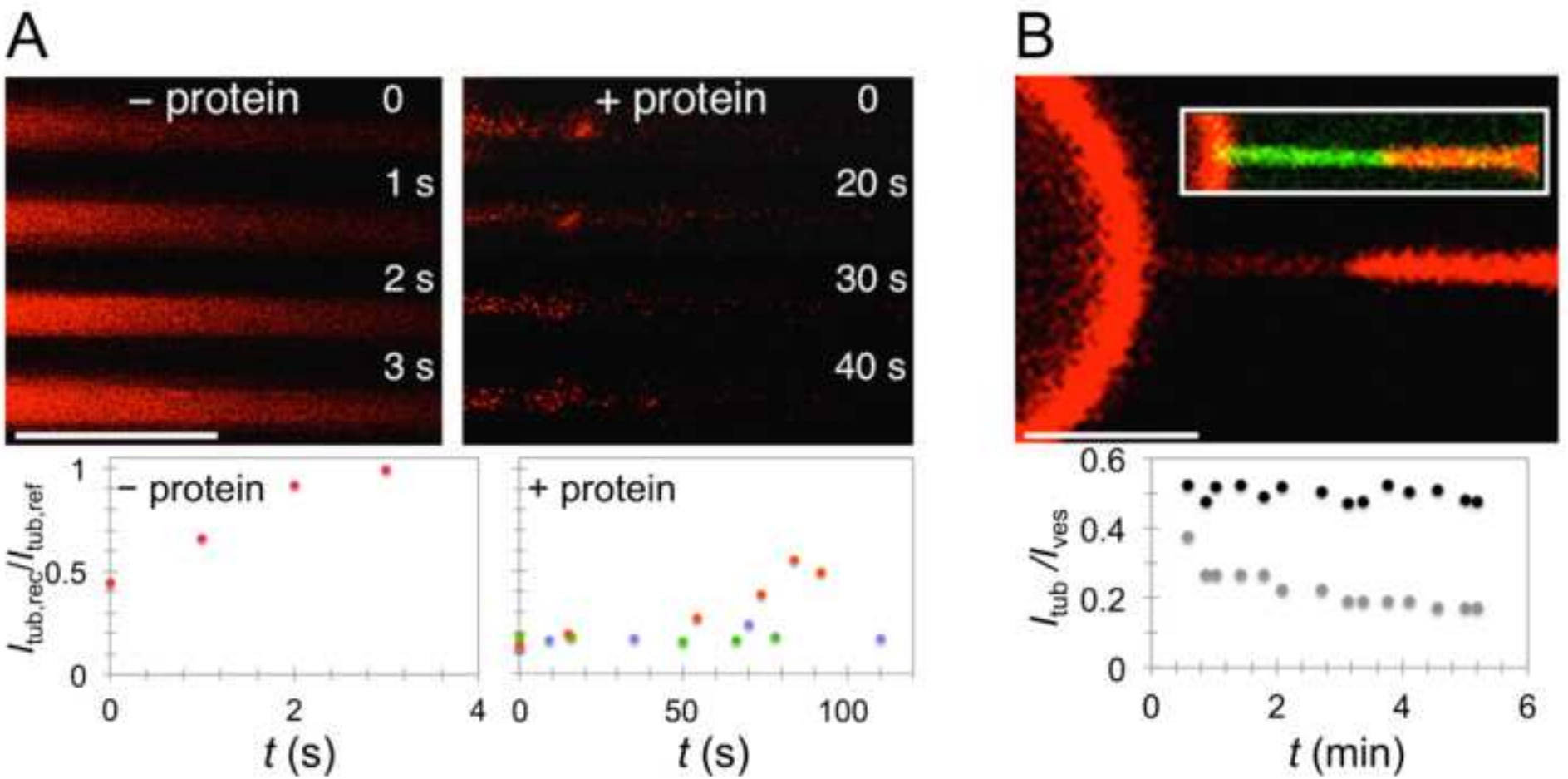

Figure 3

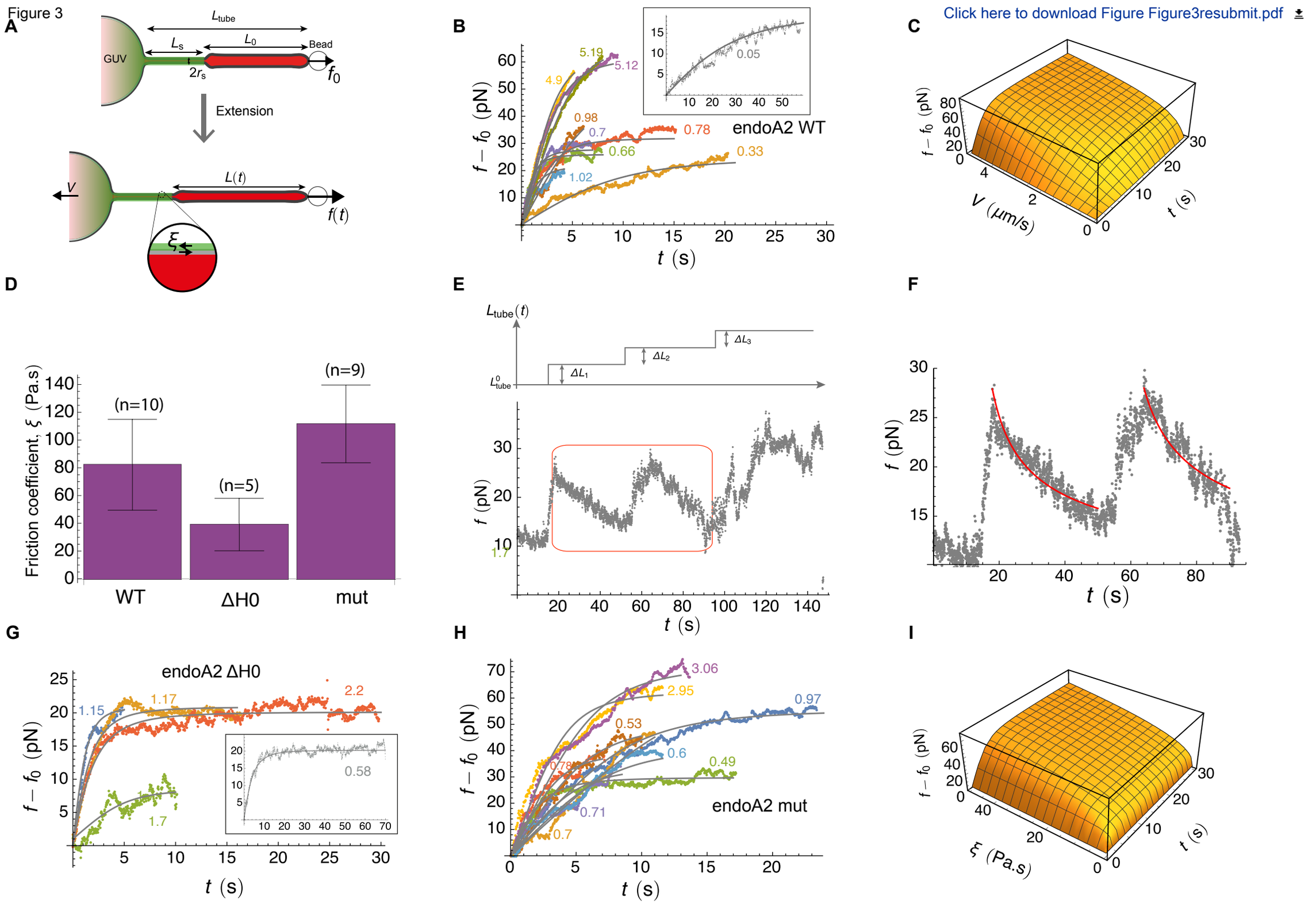

Figure 4

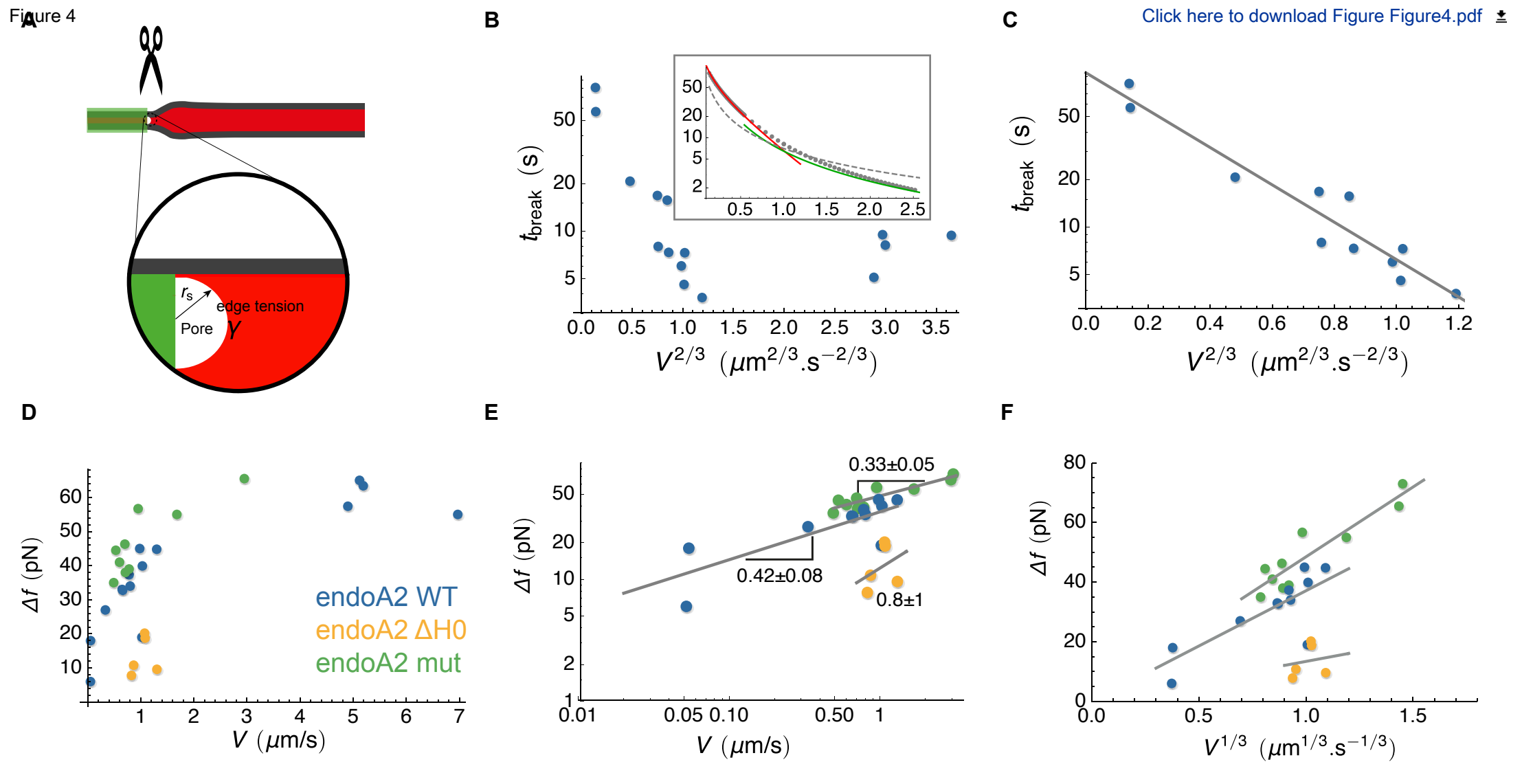

Figure 5

Click here to download Figure Figure5New.tif

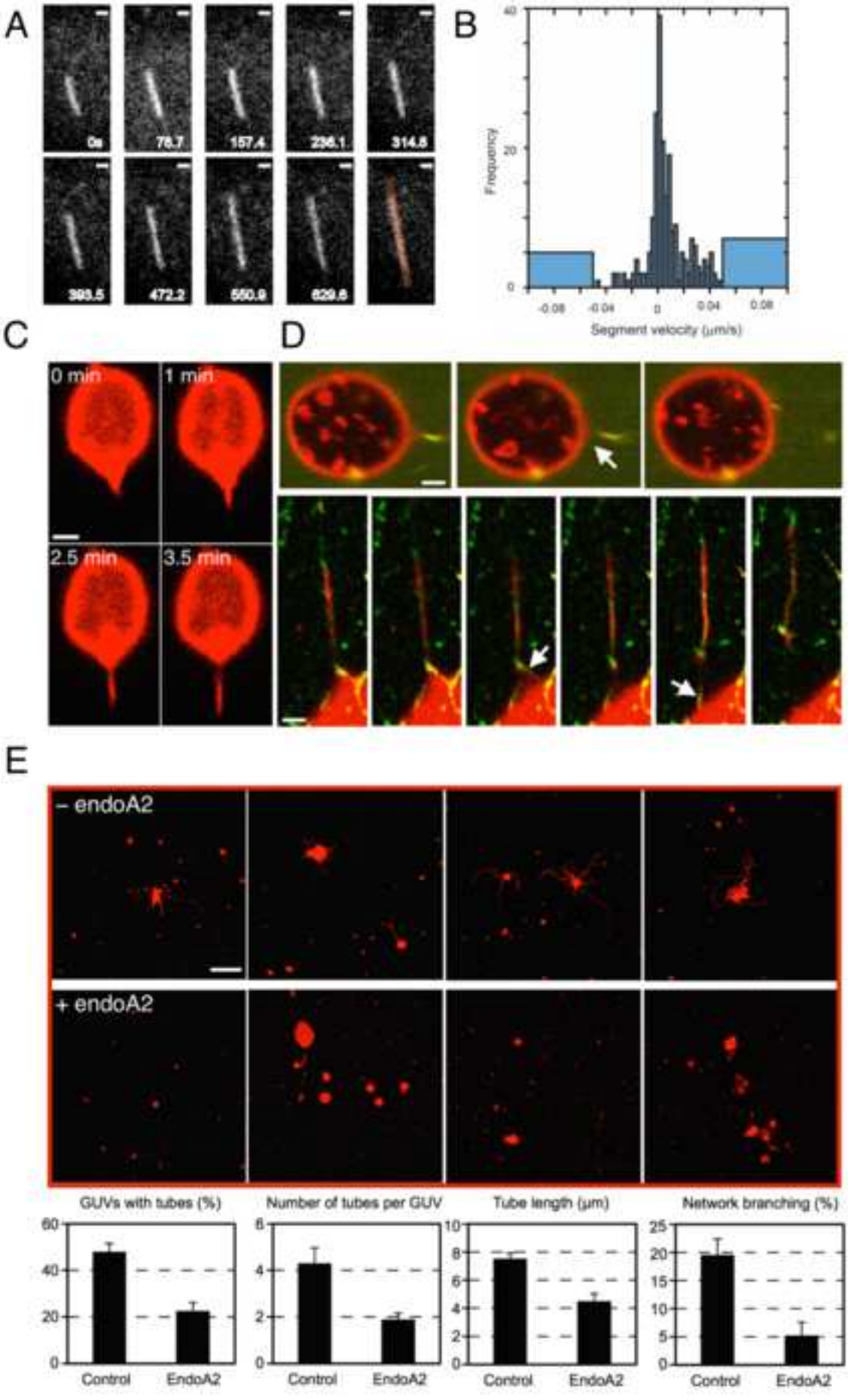

Figure 6

Click here to download Figure Figure6.tiff

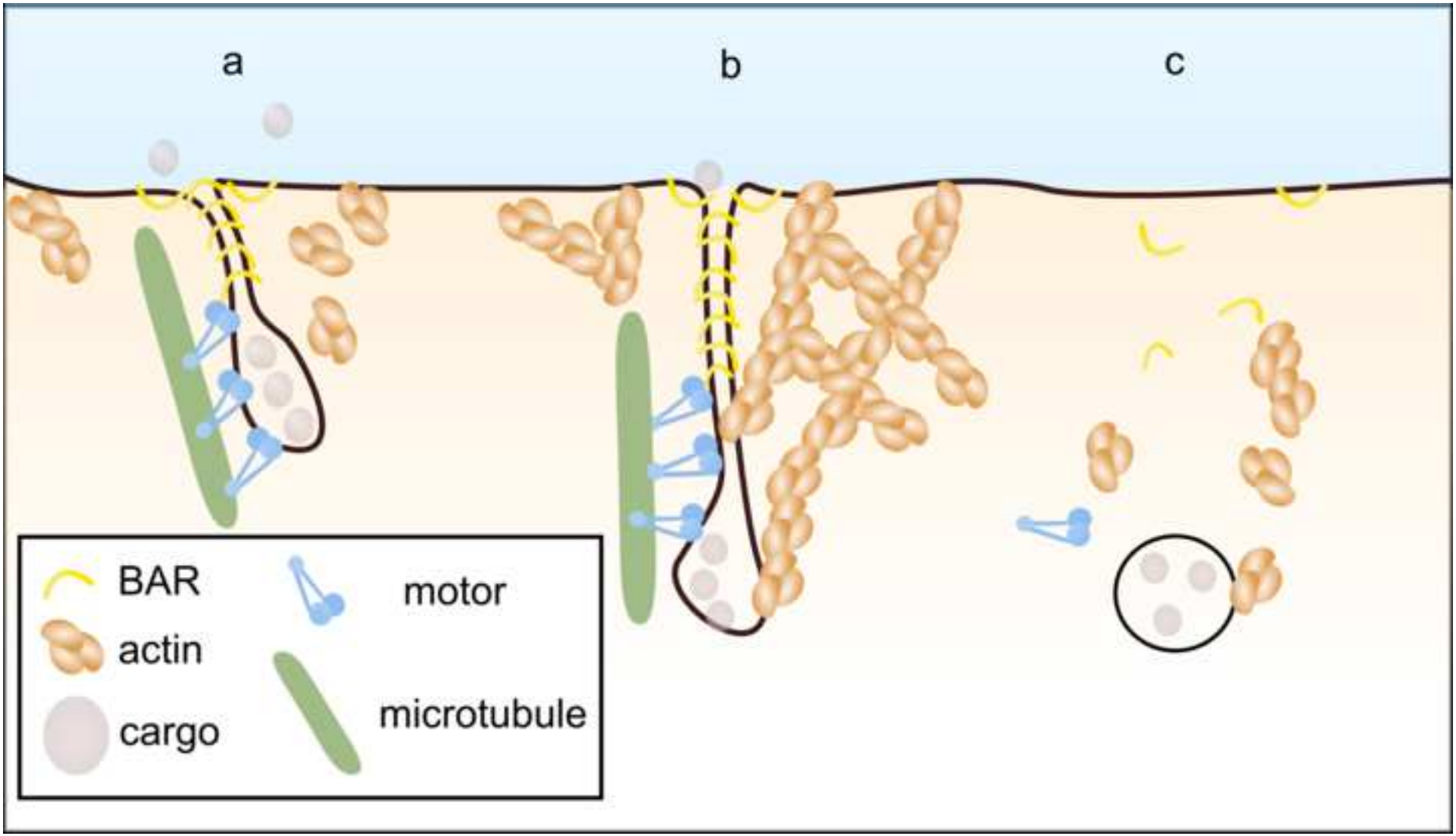

Box 1: Physics of FDS

Consider a membrane tube that is partially coated by a BAR protein scaffold (Figure). The scaffold imposes a frictional force on the underlying tube. When the tube is elongated at constant speed V, lipid flow underneath is very slow due to friction and cannot easily pass into the protein-free tube. The protein-free tube therefore becomes thinner, increasing the bending energy of the membrane. Eventually, a steady state is reached in which the flux of lipids under the protein scaffold is equivalent to the flux across the bare portion of the tube. Under these conditions, f balances the frictional force and reaches a constant value proportional to V and the friction coefficient ξ.

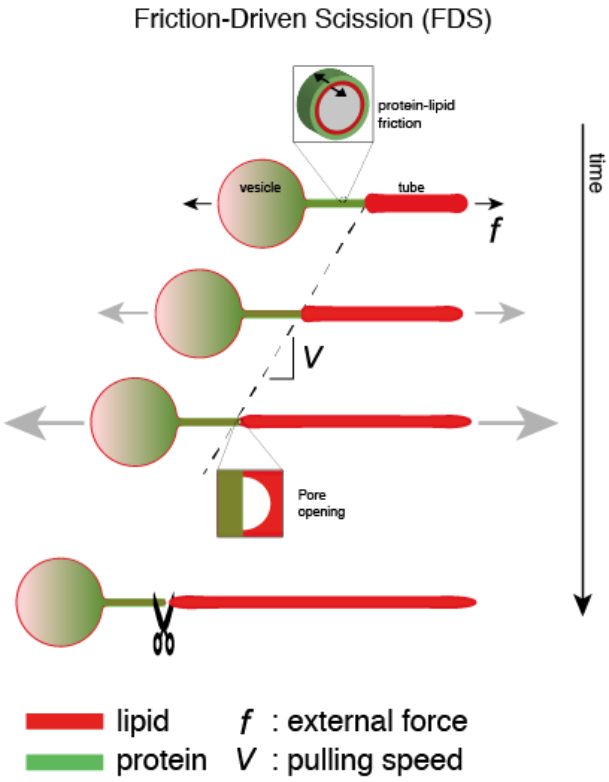

As f is further increased, so is membrane tension, σ, along the bare part of the tube, increasing the probability of a pore in the membrane leading to scission. Our model predicts that faster pulling induces FDS at a higher breaking force, f_{break}, but at a shorter time t_{break}, which we experimentally verified. Tubes scaffolded by mutated proteins whose ξ is lowered break at longer times but at lower forces than WT at comparable pulling speeds. In cells, this pulling force is likely provided by molecular motors.

Friction Mediates Scission of Membrane Nanotubes Scaffolded by BAR Proteins

Mijo Simunovic[1,2,3,1], Jean-Baptiste Manneville[4‡], Henri-François Renard[5‡,2], Emma Evergren[6,7], Krishnan Raghunathan[8], Dhiraj Bhatia[5], Anne K. Kenworthy[8], Gregory A. Voth[3], Jacques Prost[1,2,9], Harvey T. McMahon[6], Ludger Johannes[5], Patricia Bassereau[1,2*3], Andrew Callan-Jones[10*]

1. Laboratoire Physico Chimie Curie, Institut Curie, PSL Research University, CNRS UMR168, 75005 Paris, France
2. Sorbonne Universités, UPMC Univ Paris 06, 75005 Paris, France
3. Department of Chemistry, Institute for Biophysical Dynamics, James Franck Institute and Computation Institute, The University of Chicago, 5735 S Ellis Avenue, Chicago, IL 60637, USA
4. Institut Curie, PSL Research University, Subcellular Structure and Cellular Dynamics unit, CNRS UMR144, 75005 Paris, France
5. Institut Curie, PSL Research University, Chemical Biology of Membranes and Therapeutic Delivery unit, CNRS UMR3666, INSERM U1143, 75248 Paris Cedex 05, France
6. Medical Research Council Laboratory of Molecular Biology, Francis Crick Avenue, Cambridge CB2 0QH, UK
7. Centre for Cancer Research and Cell Biology, Queen's University Belfast, Belfast, UK
8. Vanderbilt School of Medicine, Department of Molecular Physiology and Biophysics, 718 Light Hall, Nashville, TN 37232, USA.
9. Mechanobiology Institute, National University of Singapore, Singapore
10. CNRS, Laboratoire Matière et Systèmes Complexes, UMR 7057, Paris, France

*corresponding authors: (lead contact) patricia.bassereau@curie.fr, andrew.callan-jones@univ-paris-diderot.fr

‡: equally contributing authors

Current addresses

[1] Center for Studies in Physics and Biology, The Rockefeller University, 1230 York Avenue, New York, USA

[2] Institut des Sciences de la Vie, Université catholique de Louvain, B1348 Louvain-la-Neuve, Belgium

[3] Lead author

Supplemental Experimental Data

The interaction of BAR proteins with membrane nanotubes

As BAR proteins, we used purified endoA2 (both full length and the N-BAR domain alone) and centaurin (BAR + pleckstrin homology (PH) domains). EndoA2 contains a BAR domain with two amphipathic helices (AHs) per monomer, whereas centaurin has a BAR domain but no helices (Peter et al., 2004).

As a model of a flat, tensed membrane, we created giant (cell-size) unilamellar vesicles (GUVs) and supported bilayers. When endoA2, its N-BAR domain alone, or centaurin were incubated at low μM concentrations with GUVs or supported bilayers, they induced spontaneous tubulation with no evidence of scission (Figures S1A–1C; Movie S1). We obtained the same results using a tensionless membrane (Figure S1). These findings are consistent with previous studies on other BAR-domain proteins (Ambroso et al., 2014; Peter et al., 2004; Sorre et al., 2012; Takei et al., 1999). Thus, all these proteins form stable tubular structures from a flat, tensed membrane, regardless of the presence of AHs—but no scission occurs.

To see if BAR proteins can cut cylindrical membranes, thus mimicking tubular membrane transport intermediates, we pulled tubes from tensed GUVs. We aspirate the GUV in a micropipette then pull out a nanotube with a micron-sized bead trapped with optical tweezers. The tube-pulling force, f, can be measured and the radius, r, can be controlled. Before proteins are added, the tube radius, r, is set by the vesicle tension, σ_v, and the membrane bending rigidity, κ, as $r = \sqrt{\kappa/2\sigma_v}$ (Derenyi et al., 2002). We explored a wide range of vesicle tensions (0.001–0.4 $mN.m^{-1}$) and thus a wide range of bare tubular radii (10–120 nm). Then, we injected the proteins near the tube at 1–5 μM (monomeric concentration in the pipette) (Simunovic et al., 2016; Sorre et al., 2012). Spontaneous scission of membrane nanotubes only occurred 4% of the time with endoA2 (N = 72) and 6% of the time with centaurin (N = 16). Instead, proteins markedly decreased the tube force, in some cases inducing buckling of membrane tubes (Figure S1D), indicating that proteins stabilize the membrane tube rather than breaking it (Renard et al., 2015). This behavior is a consequence of the formation of rigid scaffolds of BAR proteins with a tube radius larger for centaurin (40 nm) than for endoA2 (10 nm) (Simunovic et al., 2016).

FDS by centaurin scaffold

As proof of principle of a BAR protein without AHs, we tested FDS using centaurin where we observed scission events in 63% of the cases when the scaffold formed (N = 8, in the three negative cases the bead was ejected from the trap) (example plot in Figure 1). In the tested range of pulling velocities (~0.5 $\mu m.s^{-1}$), Δf of centaurin was somewhat lower than that of endoA2, 20±8 pN (at average pulling rate of 0.4±0.08 $\mu m.s^{-1}$, N = 3), compared with 31±1 pN for endoA2 in the same range of puling rates (0.5±0.1 $\mu m.s^{-1}$, N = 5). The time required for scission (in the same range of pulling rates) is significantly longer for centaurin (92±30 s) as compared to endoA2 (25±11 s).

Theoretical model

1 Introduction

We present below a theoretical description of the mechanics of a membrane nanotube coated by a protein scaffold. Our experimental measurements indicate that the force holding such a tube increases with time upon elongation, in contrast with protein-free tubes, for which the force is constant as its length changes (Derenyi et al., 2002; Koster et al., 2005). Combining these observations with the reduction in lipid mobility detected by FRAP that we found, we propose that scaffold/membrane friction opposes the relative movement of these two constituents. Based on this hypothesis, we present first a model of the tube force (Sec. 2), and then use this as input into a model of tube scission based on membrane pore nucleation (Sec. 3).

2 Theory of the force on a protein scaffolded membrane tube

When protein-scaffolded tubes were extended at constant speed V, we found that the force, $f(t)$, increased at short times after extension began, and then tended to saturate. The saturating force, f_∞, was seen to increase with V. These observations suggest a viscoelastic-like response: at short times the behavior is elastic, as lipid flow from the vesicle to the tube is impeded by friction, and f increases due to the stretching of the tubular membrane. At longer times, a balance between tube extension and lipid influx underneath the scaffold sets in, and the force becomes friction-dominated.

2.1 Force on an extended tube

To model these behaviors, we consider a tube of length $L_{\rm tube}(t)$ coated with a protein scaffold of fixed radius $r_{\rm s}$; see Figure S5. Since tubes were often found to be incompletely coated (see, for instance, Figure 1B), the total length is written $L_{\rm tube}(t) = L_{\rm s} + L(t)$, where $L_{\rm s}$ and $L(t)$ are the lengths of scaffolded and

un-scaffolded tubes (Figure 3A). The un-scaffolded tube is expected to be cylindrical, with radius $r(t)$, at distances of the order r away from the scaffold interface (Morlot et al., 2012). In cases where tubes appeared to be fully covered before extension began, such as for the tubes pulled at 50 nm.s^{-1} and 0.98 μm.s^{-1} (Figure 3B), we found that almost immediately after, gaps in the scaffold appeared (Figure S4 and Movie S3). This effectively renders the tubes incompletely coated for most of the extension period, and our hypothesis of partially coated tubes is generally valid. Upon extension, we assume that the scaffold is rigid and does not change length (see Figure 1B), and therefore $L(t) = L_0 + \Delta L(t)$, with L_0 the initial length of uncoated tube and $\Delta L(t)$ the controlled change in tube length. For constant speed extension $\Delta L(t) = Vt$ and for a sudden step, $\Delta L(t) = \Delta L_{\rm step}$.

Changing the length of a scaffolded tubes results in a time-dependent force, $f(t)$, which can be obtained by combining the following basic elements:

- First, the length of the bare part of tube is $L(t) = L_0 + \Delta L(t)$, where

$$\Delta L(t) = \begin{cases} Vt, & \text{constant speed elongation} \\ \Delta L_{\rm step}, & \text{sudden step elongation}\,. \end{cases} \tag{S1}$$

- As the tube is extended, the tension in the uncoated part of the tube is expected to increase. The tube tension is given by $\sigma(t) = K_A(A - A_0)/A_0$, where K_A is the area compressibility modulus of the membrane, $A(t)$ is the uncoated tube area, and $A_0(t)$ is the relaxed, or "preferred", uncoated area (Evans et al., 1976). During extension, $A(t)$ changes according to $dA/dt = 2\pi d(rL)/dt$. The relaxed area $A_0(t)$ changes as a result of the flux of lipids from the vesicle with speed v_l underneath the scaffold, and thus $dA_0/dt = 2\pi r_{\rm s} v_l$. Accordingly, the time derivative of σ is

$$\frac{d\sigma}{dt} = \frac{K_A}{A}\left[\frac{d}{dt}\left(2\pi rL\right) - 2\pi\, r_{\rm s}\, v_l\right]\,. \tag{S2}$$

- The total force acting along a cross-section of partially scaffolded tube is uniform, and therefore equal to the force acting on a cross-section of bare tube. This force is related to $\sigma(t)$ and the radius $r(t)$ (Dommersnes et al., 2005):

$$f = \pi\sigma r + \frac{3\pi\kappa}{2r}\,, \tag{S3}$$

where κ is the membrane bending modulus. Note that, in assuming a uniform f, we have neglected

the drag on the tube exerted by the surrounding solution. More precisely, the drag on a tube of length L and radius r is $f_{\rm drag} \simeq 2\pi\eta L\, V/\ln(L/r)$, where η is the solution viscosity (Keller and Rubinow, 1976). Taking $\eta = 10^{-3}$ Pa.s (water), $L = 5$ μm, $r = 10$ nm, and $V = 6$ μm/s (the maximum pulling speed), we find $f_{\rm drag} \approx 0.03$ pN, and thus negligible compared to the forces that we measure.

• The bare tube radius r is in turn given by a Laplace-like law across the tube membrane:

$$\Delta P = \frac{\sigma}{r} - \frac{\kappa}{2r^3}\,. \tag{S4}$$

Here, ΔP is the pressure difference between the tube interior and exterior: $\Delta P = P_{\rm t} - P_{\rm e}$. Since the connecting vesicle is very large, the pressure inside it is $P_{\rm v} \approx P_{\rm e}$, and therefore ΔP is also the pressure difference between inside the tube and inside the vesicle. It is this pressure difference that drives the flux of interior liquid during tube length changes.

• As the tube is extended, the rate of change in volume of the bare part of the tube must be equal to the liquid flux through the scaffolded region (assuming constant scaffold length):

$$\frac{d}{dt}\left(\pi r^2 L\right) = Q\,, \tag{S5}$$

where Q is the flux. Assuming Poiseuille flow underneath the scaffold, with liquid velocity v_l at $r = r_{\rm s}$, Q is given by

$$Q = \pi\, r_{\rm s}^2 \left[v_l - \frac{r_{\rm s}^2}{8\eta}\frac{\Delta P}{L_{\rm s}}\right]\,, \tag{S6}$$

• The final ingredient requires specifying a relation between the tube tension, the lipid speed v_l, and the scaffold/membrane friction. Assuming that the scaffold is mechanically coupled to the pipette (confirmed by Figure 1B), pulling on the tube generates friction between the bilayer and the coat. We propose that the tension along the bare part of the tube is

$$\sigma = \sigma_0 + \xi\, v_l\,, \tag{S7}$$

where σ_0 is the tube tension before elongation begins and ξ is the scaffold/membrane friction coefficient. Note that Equation S7 can be understood from a semi-microscopic picture in which

relative movement between membrane lipids and the scaffold results in a surface shear stress; see (Merkel et al., 1989) and further discussion in Sec. 5.

Equations S2–S7 can be solved numerically for f, σ, r, ΔP, Q and v_l. However, ΔP relaxes to zero very quickly after elongation begins, and as a result

$$r(t) \simeq \sqrt{\frac{\kappa}{2\sigma(t)}}\,, \tag{S8}$$

which is just the equilibrium bare tube radius at a tension σ (Derenyi et al., 2002). The quick relaxation of ΔP can be seen by combining Eqs. S5-S6:

$$\frac{8\eta L_{\rm s}}{r_{\rm s}^4}\frac{d}{dt}\left(r^2 L\right) = \frac{8\eta L_{\rm s}\, v_l}{r_{\rm s}^2} - \Delta P\,. \tag{S9}$$

The lefthand side and the first term on the right are both of order $8\eta L_{\rm s} V/r_{\rm s}^2 \sim 80$ Pa, assuming $\eta = 10^{-3}$ Pa·s, $L_{\rm s} = 1$ μm, $V = 1$ μm/s, and $r_{\rm s} = 10$ nm. However, the two terms contributing to ΔP [Eq. S4] are both of order $\sigma/r \sim 10^4 - 10^5$ Pa, assuming $\sigma = 10^{-4} - 10^{-3}$ N/m and $\kappa = 45\, k_{\rm B}T$ ($k_{\rm B}$ is Boltzmann's constant and T is temperature). Thus, the terms in ΔP must balance, which leads to the expression for $r(t)$, Eq. S8.

As a result of this simplication, the tube force, Eq. S3, can be written in two ways:

$$f(t) = \frac{2\pi\kappa}{r(t)} \tag{S10a}$$

$$f(t) = 2\pi\sqrt{2\kappa\sigma(t)}\,. \tag{S10b}$$

Combining these expressions with Eqs. S2 and S7 yields an autonomous equation for $f(t)$:

$$\frac{1}{8\pi^2\kappa}\frac{d}{dt}\left(f^2\right) = \frac{2\pi K_A}{A}\left[2\pi\kappa\frac{d}{dt}\left(\frac{L}{f}\right) - \frac{f^2 - f_0^2}{8\pi^2\kappa\,\xi/r_{\rm s}}\right], \tag{S11}$$

where $f_0 = 2\pi\sqrt{2\kappa\sigma_0}$ is the tube force before elongation begins.

A final simplification can be made. Comparing the df/dt terms on the left and right sides above shows that the lefthand side is negligible for forces $f < \left(\frac{32\pi^4\kappa^2 K_A L}{A}\right)^{1/3}$. Taking $K_A = 200$ mN/m (Rawicz et al., 2000), $A = 2\pi r L \sim 0.3$ μm^2, and $L = 5$ μm, we find that this condition requires $f \lesssim 700$ pN, which is much larger than the forces that we measure. Thus, the terms on the righthand side above must

balance, implying $A(t) \simeq A_0(t)$, or that the membrane tube is essentially incompressible. As a result, we obtain

$$\frac{d}{dt}\left(\frac{L}{f}\right) = \frac{r_{\rm s}}{16\pi^3\kappa^2\xi}\left(f^2 - f_0^2\right) . \tag{S12}$$

Equation S12 is the central equation of our model and can be solved to find f for different pulling protocols, such as given by Eq. S1.

2.2 Constant speed elongation

For a constant speed elongation experiment [Eq. S1], we see directly from Eq. S12 that at long times after elongation begins, f saturates to a value f_∞ obtained by solving the cubic equation

$$f^3 - f_0^2\, f - 16\pi^3\kappa^2\xi\, V/r_{\rm s} = 0\,, \tag{S13}$$

and thus, for large V,

$$f_\infty \simeq \left(16\pi^3\kappa^2\xi\, V/r_{\rm s}\right)^{1/3} ; \tag{S14}$$

see also Eq. 5 in the main text. Equation S13 is almost identical to an equation obtained for pulling tubes from plasma membranes that experience friction with membrane-cortex linking proteins (Brochard-Wyart et al., 2006). Note that in the problem studied in (Brochard-Wyart et al., 2006), the tube is bare, its radius is uniform, and thus every point on it moves at the same speed, equal to the constant pulling speed V; as a result, the force is time-independent. In our case, however, the tube scaffold friction prevents lipids underneath it from flowing instantly when elongation begins, and thus initially $v_l = 0$. Gradually, v_l increases, giving rise to the time dependence of f. Finally, we note that the scaling of f_∞ with $V^{1/3}$ can be understood simply since $f^2 \propto \sigma \propto v_l$, while by mass conservation at steady state, $v_l = V r_\infty/r_{\rm s}$, with a limiting value of the uncoated tube radius $r_\infty \propto 1/f_\infty$ [Eq. S10a]; therefore, $f_\infty^3 \propto V$, or $f_\infty \propto V^{1/3}$.

Equation S12 can be integrated for $L = L_0 + Vt$, and after considerable algebra an implicit expression for f can be obtained. Defining the characteristic time

$$\tau_{\rm r} = \frac{16\pi^3\kappa^2\xi L_0}{r_{\rm s} f_0^3} \tag{S15}$$

(it will be seen later to be related to the force relaxation time after a step length jump) and re-scaling time, pulling speed, and force according to $t' = t/\tau_{\rm r}$, $V' = V\tau_{\rm r}/L_0$, and $f' = f/f_0$, Eq. S12 can be re-written

as

$$\frac{\dot{f}'}{f'} = -\frac{f'^3 - f' - V'}{1 + V't'}\,, \tag{S16}$$

where the overdot denotes differentiation with respect to t'. After some calculation we find

$$f' \prod_{n=1}^{3} \left(\frac{1 - a_n}{f' - a_n} \right)^{\frac{a_n^2 - 1}{3a_n^2 - 1}} = 1 + V't'\,, \tag{S17}$$

where

$$\begin{aligned} a_1 &= \frac{2 \cdot 3^{1/3} + 2^{1/3}\alpha^{2/3}}{6^{2/3}\alpha^{1/3}} \\ a_2 &= -\frac{1 + i\sqrt{3}}{2^{1/3}3^{1/3}\alpha^{1/3}} - \frac{\left(1 - i\sqrt{3}\right)\alpha^{1/3}}{2^{4/3} \cdot 3^{2/3}} \\ a_3 &= a_2^*\,. \end{aligned} \tag{S18}$$

In the above, $i = \sqrt{-1}$, the asterisk denotes complex conjugation, and

$$\alpha = 9V' + \sqrt{81V'^2 - 12}\,. \tag{S19}$$

Fortunately a useful simplification can be made, since $\alpha \gg 1$—that is, even at the lowest pulling speed, roughly 50 nm/s, $V' = 16\pi^3\kappa^2\xi\, V/(r_s f_0^3) \approx 3$, assuming $f_0 = 10$ pN, $\xi = 50$ Pa.s (see main text, Table 1), and thus $\alpha \approx 50$. In the limit $\alpha \gg 1$, Eq. S17 can be shown to simplify to the cubic equation

$$f'^3 - a(t')f' - V'a(t') = 0 \tag{S20}$$

where $a(t') = \left[1 + V'/(1 + V't')^3\right]^{-1}$. The positive real root to this equation can be readily found, though its expression in terms of t' and V' is cumbersome. Instead, a very good approximate formula valid for $V' \gg 1$ can be obtained, namely $f' \simeq (V'a)^{1/3}$, which leads to

$$f(t) = f_0 \frac{1 + Vt/L_0}{\left[1 + \frac{(1+Vt/L_0)^3}{16\pi^3\kappa^2\xi V/(r_s f_0^3)}\right]^{1/3}}\,; \tag{S21}$$

see also Equation (3) of the main text. Equation S21 reveals two distinct force regimes that are consistent

with our experiments: for times $t < t^*$, where

$$t^* = \left(\frac{16\pi^3 \kappa^2 \xi L_0^3}{r_\mathrm{s} f_0^3 V^2} \right)^{1/3} , \tag{S22}$$

f increases from f_0 linearly with time, whereas for $t > t^*$ tends to saturate to f_∞. Equation S21 was then used to fit experimental force data (Figure 3), allowing us to extract the friction coefficient ξ for endoA2 WT, endo ΔH0, and endo mut. Note that the bare tube length prior to elongation, L_0, is difficult to measure experimentally, and was handled as a second fit parameter.

2.3 Force relaxation after a jump in tube length

How the tube force relaxes after a sudden change in tube length, ΔL_step, provides a second way to probe scaffold/membrane friction. Prior to the length change, assumed to occur at $t = t_0$, we have $L = L_0$ and $f = f_0$; right after the jump, $L = L_0 + \Delta L_\mathrm{step}$ and $f = f_\mathrm{peak}$. The peak force, f_peak is found by integrating Eq. S12 from $t = t_0 - \epsilon$ to $t_0 + \epsilon$, with ϵ the short period over which the step is applied. This leads to

$$\frac{L_0}{f_0} = \frac{L_0 + \Delta L_\mathrm{step}}{f_\mathrm{peak}} . \tag{S23}$$

Experimentally, ΔL_step is controlled and f_peak can be measured directly, whereas L_0 is unknown. The above equation, however, can be solved to infer L_0:

$$L_0 = \frac{\Delta L_\mathrm{step}}{f_\mathrm{peak}/f_0 - 1} . \tag{S24}$$

With this knowledge, the force relaxation curve can be calculated by solving the following variant of Eq. S12:

$$\frac{df}{dt} = -\frac{r_\mathrm{s}}{16\pi^3 \kappa^2 \xi (L_0 + \Delta L_\mathrm{step})} f^2 \left(f^2 - f_0^2 \right) , \tag{S25}$$

with the initial condition $f(t_0) = f_\mathrm{peak}$. While this differential equation is non-linear, for small $\Delta L_\mathrm{step} = \delta L$, we can write $f = f_0 + \delta f$ and the righthand side above can be linearized, yielding

$$\frac{d\delta f}{dt} \simeq -\frac{2}{\tau_\mathrm{r}} \delta f , \tag{S26}$$

where the characteristic time τ_r, given by Eq. S15, appears. Therefore, this quantity is closely related to the relaxation time constant for the force after a sudden length change. Equation S25 was then used to fit

our force relaxation data, yielding another determination of ξ.

3 Model of tube scission through membrane pore nucleation

3.1 Energy barrier for pore nucleation

In this last section, we develop a model of tube scission resulting from the friction-driven force increase discussed above. The proposed scission mechanism involves membrane pore nucleation and growth at sufficient tension, a process which has been studied in synthetic membrane systems (Evans et al., 2003). When extended at constant speed V, we found that endoA2-coated tubes broke at a time $t_{\rm break}$ that decreases with increasing V (Figure 4B). This suggests that tube scission involves thermal activation over a barrier that is lowered by the applied force.

To model this, we assume heterogeneous membrane pore nucleation, occurring at the boundary between the bare tube and the scaffold [1]; once the pore size reaches the scaffold radius $r_{\rm s}$, scission occurs. Pore nucleation involves passing an energy barrier, which in the context of a membrane tube subject to a force f is given by the change in the thermodynamic function (Landau and Lifshitz, 1986)

$$\Phi = F_{\rm tube} - fL \tag{S27}$$

for a segment of bare tube of length L . Once a pore forms, assumed to be semi-circular with radius a, rupture costs energy because a membrane edge is exposed; this cost is equal to $\gamma\pi a$, where γ is the edge tension (Evans et al., 2003). In addition, upon pore formation the tube must elongate a bit to accommodate the area $\pi a^2/2$. Since the tube area is conserved, the change in length is given by $\Delta L = (\pi a^2/2)/(2\pi r) = a^2/4r$; this contributes to $\Delta\Phi$ a term $-f\Delta L = -fa^2/4r = -f^2a^2/(8\pi\kappa)$, where Eq. S10a has been used. Finally, also because of area conservation and because the tube radius r is constant (since f is assumed constant), the bending contribution to $F_{\rm tube}$ is unchanged. Therefore, the barrier for nucleating a pore of size a, which we denote $W_a = \Delta\Phi$, is given by

$$W_a(t) = \gamma\pi a - \frac{f(t)^2a^2}{8\pi\kappa}\,. \tag{S28}$$

Note that, in principle, the pore radius is variable and the probability of nucleating one with radius a

[1] Heterogeneous, as opposed to homogeneous, nucleation requires exposing less free membrane edge, thus costing lower energy.

depends on W_a. At a given value of f, as usual in nucleation theory, W has a maximum for a given $a = a_c$, and in our case occurs at $a = a_c = 4\pi^2\kappa\gamma/f^2$: pores with $a < a_c$ re-seal, while those with $a > a_c$ grow. We note that for bare membranes $\gamma \sim 10$ pN (Evans et al., 2003), but is significantly reduced in the presence of proteins; see, for example, (García-Sáez et al., 2007; Lee et al., 2008) . Thus, assuming $\gamma = 3$ pN, and $f = 30$ pN, we find that $a_c \approx 25$ nm, and thus greater than $r_s \approx 10$ nm. This means that pores that spontaneously form with $a < r_s$ will not grow and lead to scission, and the only scission-relevant pores are those with radius r_s. Therefore, the relevant energy barrier is

$$W(t) = \gamma\pi r_s - \frac{f(t)^2 r_s^2}{8\pi\kappa} . \tag{S29}$$

In the following, we separate the force-dependent and independent parts of W as $W = W_0 + W_f$, where

$$W_0 = \pi r_s \gamma \tag{S30}$$

and

$$W_f(t) = -\frac{r_s^2\, f(t)^2}{8\pi\kappa} . \tag{S31}$$

We next calculate the tube scission (or rupture) probability from W and use it to determine $t_{\rm break}$ and the breaking force, $f_{\rm break}$, as functions of V.

3.2 Scission probability

To calculate the scission probability, we apply Kramers' theory for thermally activated processes (Kramers, 1940). Applying this theory, valid for large barriers compared with $k_B T$ (k_B is Boltzmann's constant and T is temperature), the force-dependent pore nucleation rate, $\nu(t)$, can be written

$$\nu(t) = \nu_0 \exp\left(-\frac{W_f(t)}{k_B T}\right) . \tag{S32}$$

In the above, $\nu_0 = \bar{\nu}\exp\left(-\frac{W_0}{k_B T}\right)$, where $\bar{\nu}$ is a constant that depends on edge tension, thermal energy, and hydrodynamic drag and is on the order of 10^6 Hz (Evans et al., 2003). Following the general arguments in (Evans et al., 1991; Evans and Ritchie, 1997; Evans et al., 2003), the probability that rupture

occurs between t and $t + dt$ is

$$P(t) = \nu(t) \exp\left[- \int_0^t \nu(t')dt' \right] , \tag{S33}$$

where $\exp\left[- \int_0^t \nu(t')dt' \right]$ is the probability that the tube has remained intact up to time t.

The probability $P(t)$ allows us to calculate $t_{\rm break}$, which we identify with the most probable value of $P(t)$. Noting that $P(t)$ can be expressed as $P(t) = \exp\left[\ln \nu(t) - \int_0^t \nu(t')dt' \right]$, $dP/dt = 0$ occurs at a time t obtained by solving

$$\left. \frac{d \ln \nu}{dt} \right|_{t=t_{\rm break}} = \nu(t_{\rm break}) \, . \tag{S34}$$

Using Eqs. S29 and S32 the above can be re-written as

$$\frac{2}{\nu_0 \bar{f}^2} f \dot{f} = e^{f^2/\bar{f}^2} \qquad \text{at } t = t_{\rm break} \, , \tag{S35}$$

where $\bar{f}^2 = 8\pi\kappa/r_{\rm s}^2$. Thus, by solving Eq. S35 using the explicit expression for $f(t)$, Eq. S21, $t_{\rm break}$ can be found, as well as the breaking force $f_{\rm break} = f(t_{\rm break})$. These operations determine the scission statistics as a function of V. Generally, Eq. S35 must be solved numerically, though as we calculate below, fairly simple asymptotic expressions for $t_{\rm break}$ and $f_{\rm break}$ can be obtained in limiting cases.

3.3 Expressions for breaking time and force

As represented in the inset of Figure 4B, analytical expressions for $t_{\rm break}$ and $f_{\rm break}$ can be obtained for the two force regimes, $t_{\rm break} > t^*$ and $t_{\rm break} < t^*$. For $t_{\rm break} \gg t^*$, that is, for low V (made more precise below), f is approximately saturated, thus $f = f_{\rm break} \simeq f_\infty$. Noting that Eq. S21 can be written

$$f(t) = f_\infty \frac{1 + t/t^*}{\left[1 + (t/t^*)^3\right]^{1/3}} \, , \tag{S36}$$

in the low V regime the time derivative in Eq. S35 is $df/dt \simeq f_\infty t^{*3}/t^4$. Therefore, Eq. S35 becomes

$$\frac{2 f_\infty^2}{\nu_0 \bar{f}^2} \frac{t^{*3}}{t^4} = e^{f_\infty^2/\bar{f}^2} \, , \tag{S37}$$

which yields

$$t_{\rm break} \simeq \tau \exp\left[- \frac{\pi}{k_B T} \left(\frac{\kappa \xi^2 V^2 r_{\rm s}^4}{128} \right)^{1/3} \right] ; \tag{S38}$$

see also Eq. 6 of the main text. In the above equation, the time constant is given by

$$\tau = \frac{2^{7/6}\,\pi\left(\kappa^7\xi^5 r_{\rm s}\right)^{1/12}}{V^{1/3}}\left(\frac{L_0^3}{f_0^3 k_{\rm B}T\nu_0}\right)^{1/4}. \tag{S39}$$

In the opposite limit, $t_{\rm break} \ll t^*$, $f \simeq f_0\,(1 + Vt/L_0)$, and therefore Eq. S35 can be written

$$\frac{2Vf_0 f}{\nu_0 L_0 \bar{f}^2} = e^{f^2/\bar{f}^2}. \tag{S40}$$

Therefore, for large V,

$$f_{\rm break} \simeq \bar{f}\sqrt{\ln\left(\frac{2Vf_0^2}{\nu_0 L_0 \bar{f}^2}\right)}. \tag{S41}$$

and

$$t_{\rm break} = \frac{L_0}{V}\left(\frac{f_{\rm break}}{f_0} - 1\right). \tag{S42}$$

We note that the crossover value of V between the two regimes is found roughly by equating the expressions in Eq. S38 and S42; see also the inset of Figure 4B. Assuming $\xi = 50$ Pa.s, $f_0 = 10$ pN, $\gamma = 3$ pN, and $L_0 = 1$ μm, we find that this value is $V \approx 1$ μm/s. Since most of our scission data occurs for pulling speeds less than this value, we therefore used Eq. S38 to fit the measured breaking times, thereby yielding another estimate of ξ; see Figures 4C, 4E, and 4F.

Note finally that the expressions obtained here for $t_{\rm break}$ and $f_{\rm break}$ depend on $P(t)$ having a narrow peak and on the assumption $\alpha \gg 1$ that underpins Equation S21; see Sec. 2.2. Thus, these expressions break down for small ξ, which can be seen from the unphysical result that $t_{\rm break} \to 0$ for $\xi \to 0$ in Eq. S38. As argued above in Sec. 2.2, our experimental data indicate that $V' > 1$ and $\alpha \gg 1$, thus validating the approximations leading to the expressions in this section.

3.4 Note on other scission mechanisms

We have considered above a model of tube scission that depends on membrane pore nucleation. Two other routes to scission are possible, which we discuss below. We show that these are not applicable to BAR protein-mediated tube scission, which occurs on a seconds-to-minutes time scale.

First, local tube pinching from a radius r_0 down to $r_i \approx 3$ nm can lead to scission via a hemifission intermediate state (Kozlovsky and Kozlov, 2003). The corresponding energy barrier is $\Delta E \approx \pi^2\kappa^2\left(r_i^{-1} - r_0^{-1}\right)/f$ (Morlot et al., 2012). In the case of dynamin-assisted scission, GTP hydrolysis

constricts the dynamin coat down to $r_0 \approx 4.5$ nm, thereby significantly lowering the energy barrier. In contrast, r_0 for endoA2-scaffolded tubes is much larger: the scaffold radius itself is 10 nm (Simunovic et al., 2016; Renard et al., 2015), and the adjacent bare membrane tube, even at the highest attained forces, around 70 pN, has a radius no smaller than ∼15 nm; see Eq. S10a. Thus, in our case, $\Delta E \approx 250\, k_{\mathrm{B}}T$. This energy corresponds to a scission time of $\tau \exp(\Delta E/k_{\mathrm{B}}T) \approx 10^{96}$ hours, where $\tau \sim 10^{-9}$ s (Morlot et al., 2012), and thus impossible!

Secondly, it has been proposed that line tension, which arises at the boundary between lipid domains and acts to reduce the boundary length, could constrict tubes enough to cause scission (Allain et al., 2004; Römer et al., 2010). For tubes that are partially coated by a BAR domain scaffold, Liu et al proposed that sequestration of PI(4,5)P2 by the scaffold results in a line tension at the interface with the bare membrane (Liu et al., 2009). In contrast with their model of endocytosis, in which enzymatic activity amplifies PI(4,5)P2 concentration differences, in our case the PI(4,5)P2 enrichment under the coat is limited to a factor of three (Picas et al., 2014), and thus, according to (Liu et al., 2009), a line tension of $\lambda \approx 5$ pN. As a result, tube scission would release an energy $2\pi\lambda r_{\mathrm{s}} \approx 78\, k_{\mathrm{B}}T$, and our above estimation for the energy barrier would be reduced to $170\, k_{\mathrm{B}}T$. This barrier is still too great to be passed over by thermal processes on any reasonable timescale, and we thus rule it out.

4 Note on why different measurements yield different values of the friction coefficient

Here, we briefly comment on the different ways to estimate the protein/lipid friction coefficient, ξ (Table 1), and why these lead to different values. The first way of estimating ξ was from individual fits to the force versus time data sets (Table 1, first row). For each protein type (endoA2 WT, endoA2 mut, and endoA2 ΔH0), a number n of data sets were fitted, from each of which a value of ξ was obtained through Eq. S21. We note that each f vs t set comes from a single pulling experiment, with a given protein scaffold (and thus given length, L_{s}). The reported value of ξ for each protein was the average over the n fitted data sets.

In contrast, the values of ξ given in the second and thirds rows of Table 1 were obtained from fits to the scission data set (force at breakage versus V and time until breakage vs. V), each point in the set corresponding to a different pulling experiment. As a result, the manner in which the data were averaged is not the same as described above. (We note, however, that the values obtained from f_{break} vs. V and

$t_{\rm break}$ vs. V are within the margin of error for endoA2 WT). These two different averaging methods result in different values of ξ values because of variability in scaffold properties from one experiment to another. This is one reason for the discrepancy in the values of ξ for a given protein type between the different estimation methods.

A second reason for the discrepancy could be related to our model of pore nucleation leading to scission. Namely, we assume that a semi-circular pore of radius equal to that scaffold nucleates at the scaffold/bare tube interface. Considering the tubular geometry, this might be an approximation to reality; nevertheless, a careful description of the pore shape is beyond the scope of this manuscript.

5 Note on sources of protein/lipid friction and tension along tube

We briefly justify here the expression for the tube tension as a function of lipid velocity, Eq. S7. If we consider the force balance on a cylindrical element of lipid bilayer, of constant radius, underneath the protein scaffold, we obtain

$$\frac{\partial \sigma}{\partial z} = \zeta v_l \,, \tag{S43}$$

where ζ is an intensive friction coefficient and σ is the local tension. Integrating this expression from $z = 0$ (base of the scaffold, assumed to coincide with tube neck) to $z = L_{\rm s}$ (scaffold length), we recover Eq. S7, where we identify ξ as $\zeta L_{\rm s}$ and σ_0 as the tension on the vesicle.

There is, however, another source of protein/lipid friction that complicates the above picture. Namely, since the scaffold is anchored to the GUV (note Figure 1B, for example, where the scaffold is seen to move with the displaced GUV), there must be additional dissipation. This most likely comes from friction between lipids and proteins at the tube neck, and possibly over an extended part of the GUV. As a result, we expect that ξ can be written $\xi = \zeta L_{\rm s} + \xi'$, where ξ' is independent of the scaffold length. It is difficult to estimate ξ', though one line of reasoning goes as follows. As the tube is pulled, the neck presents a barrier of width $\sim r_{\rm s}$ to tube-directed lipids from the GUV. Since ξ' is dimensionally given by a force per unit area multiplied by time, at the scaling level, it can be estimated as the force per unit area acting on lipids as they pass the neck, times the barrier crossing time. Thus,

$$\xi' \sim \frac{W_{\rm n}}{e^2 r_{\rm s}} \tau_0 \, e^{\frac{W_{\rm n}}{k_{\rm B}T}} \,, \tag{S44}$$

where e is the bilayer thickness, τ_0 is the lipid diffusion time over a distance $r_{\rm s}$, and $W_{\rm n}$ is the barrier

height. Taking the lipid diffusion constant $D = 10^{-12}$ m^2/s, $r_\mathrm{s} = 10$ nm, and $e = 5$ nm, we obtain $\xi' \sim$ (1 Pa.s) $W_\mathrm{n}/(k_\mathrm{B}T)\exp(W_\mathrm{n}/k_\mathrm{B}T)$. Thus, for ξ' to be of the same order as ζL_s ($\approx$ 50 Pa.s), the barrier height need only be on the order of a few $k_\mathrm{B}T$. This barrier height is not that high, and this argument likely explains why assigning all the friction to ζL_s is inaccurate.

Finally, we point out recent work suggesting that the stiffness and spontaneous curvature of a localized protein patch influence the tension on a membrane (Rangamani et al., 2014; Walani et al., 2015; Hassinger et al., 2017). These studies consider the mechanics of a composite protein plus lipid membrane with inhomogeneous material properties. Recall that in our experiments, the protein scaffold is assumed to be a fixed, rigid cylindrical coat that does not change in time. As a result, in the model we only consider the dynamics of the lipid bilayer flowing under this fixed coat, and relate its tension to the lipid flow. Even if the scaffold's bending ridigity and intrinsic curvature affect the tension, according to Ref. (Rangamani et al., 2014), since the scaffold's material properties are assumed to remain constant in time, the influence on tension does not change with time, and cannot explain the tension "build-up" that can be inferred from the tube pulling force, generated externally. Thus, in our case, it is not necessary to use a formalism, such as presented in Ref. (Rangamani et al., 2014), that focuses on the composite membrane (proteins and lipids together).

This is in contrast with Ref. (Hassinger et al., 2017), in which a composite membrane description is appropriate, since the coat formed by clathrin proteins is not fixed, and for which the shape of the protein plus lipid membrane evolve together as a result of localized spontaneous curvature and bending rigidity.

Supplemental Figure 1

Click here to download Supplemental Figure FigureS1.tif

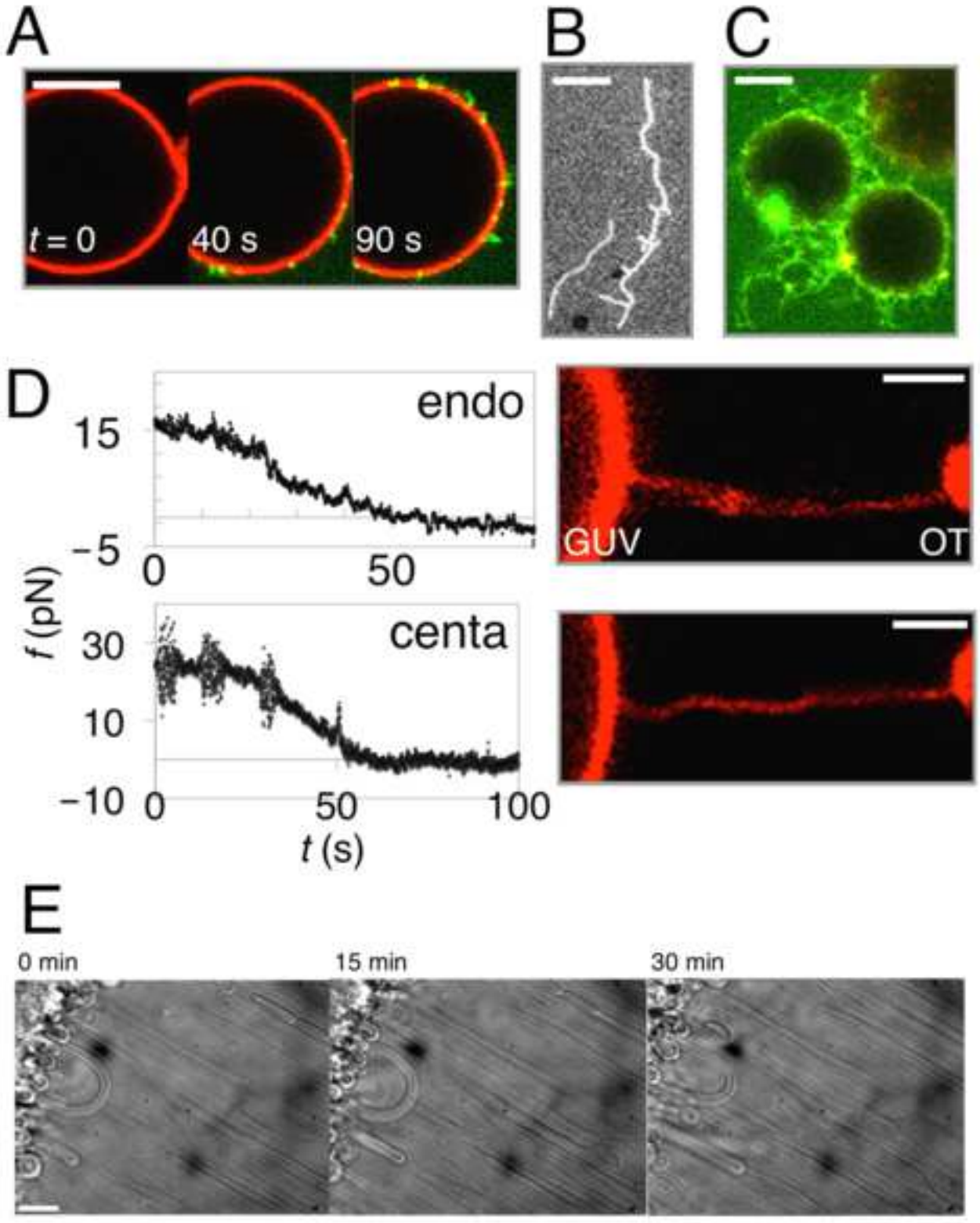

Supplemental Figure 2

Click here to download Supplemental Figure FigureS2.tiff

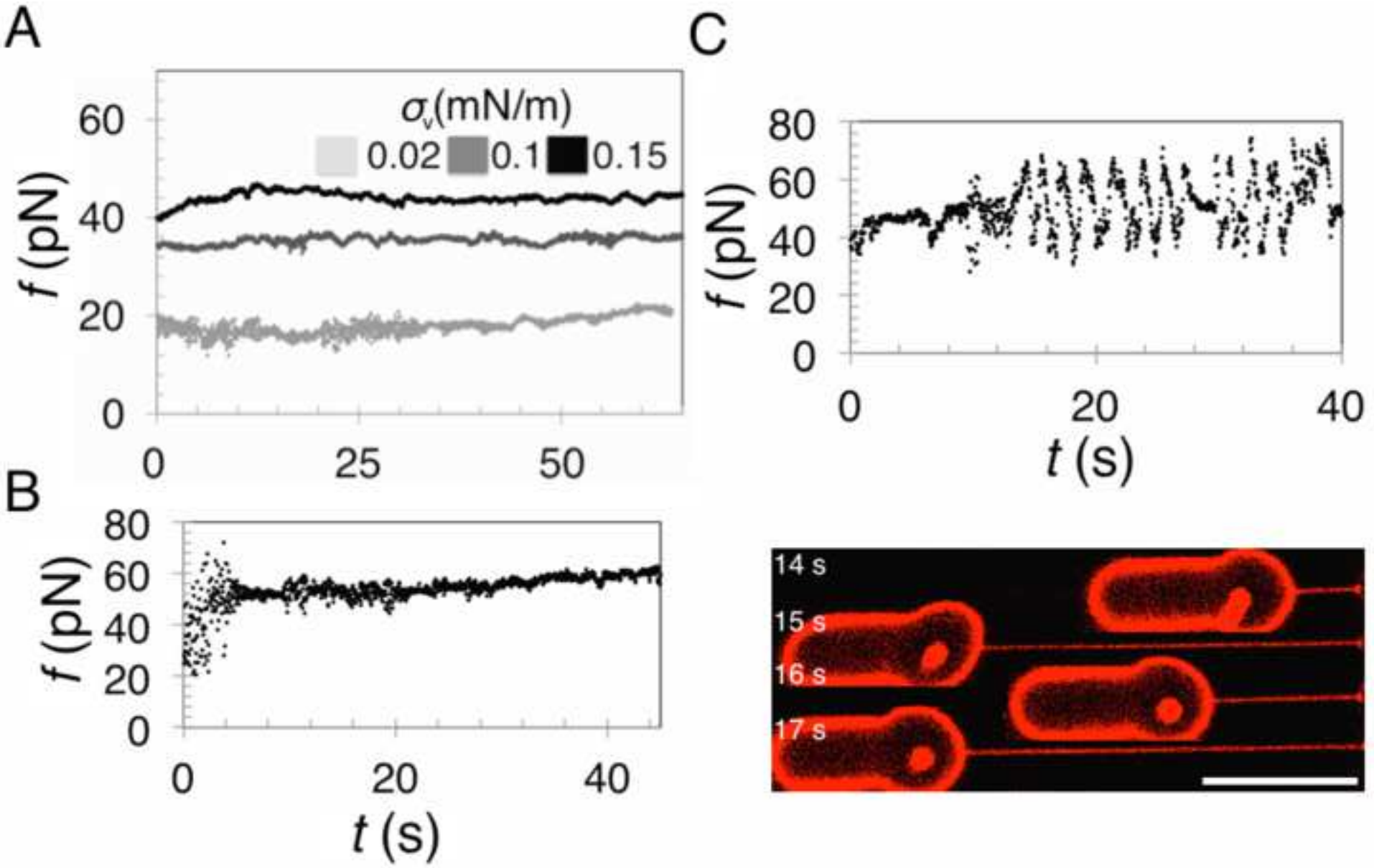

Supplemental Figure 3

Click here to download Supplemental Figure FigureS3.tiff

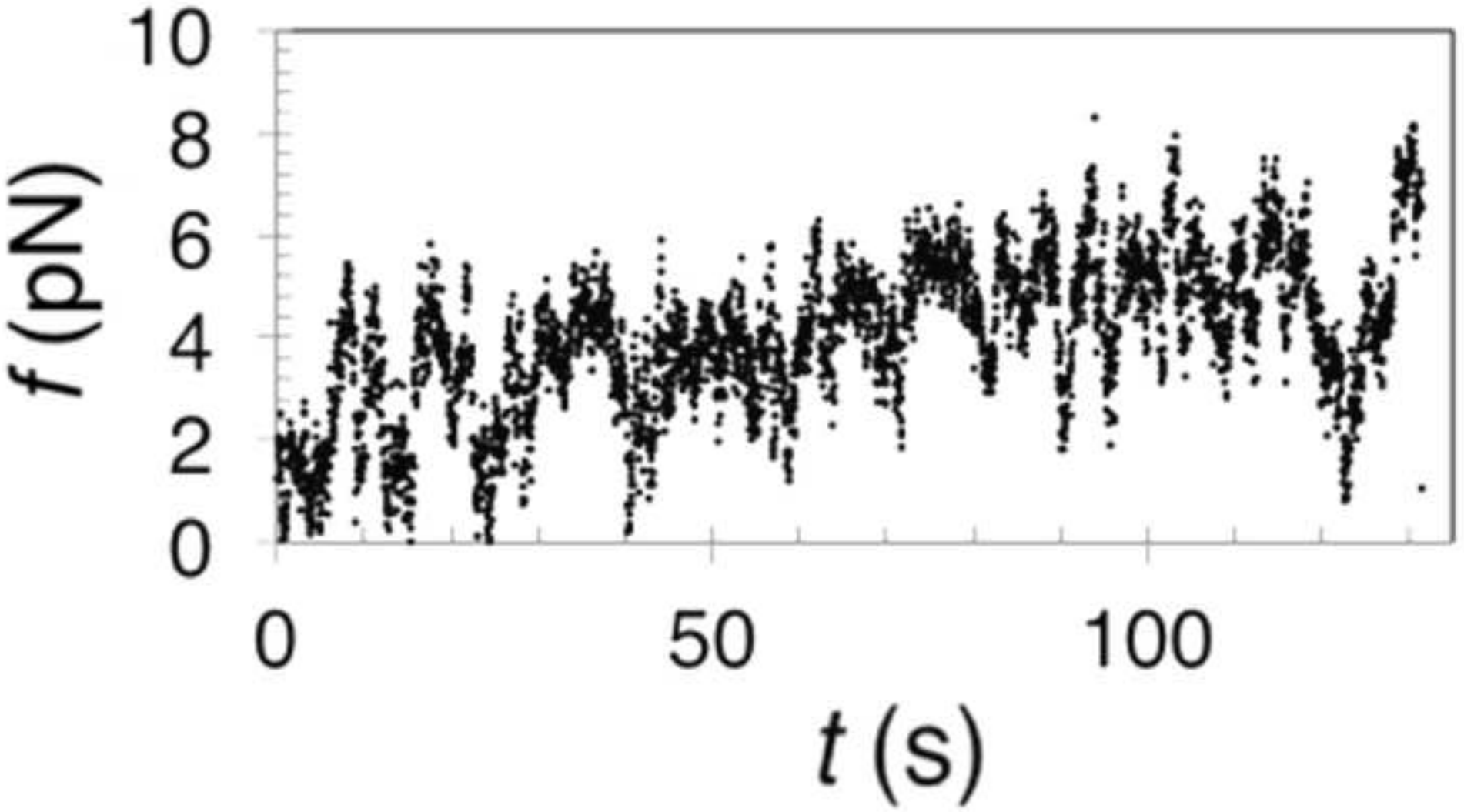

Supplemental Figure 4

Click here to download Supplemental Figure FigureS4.tif

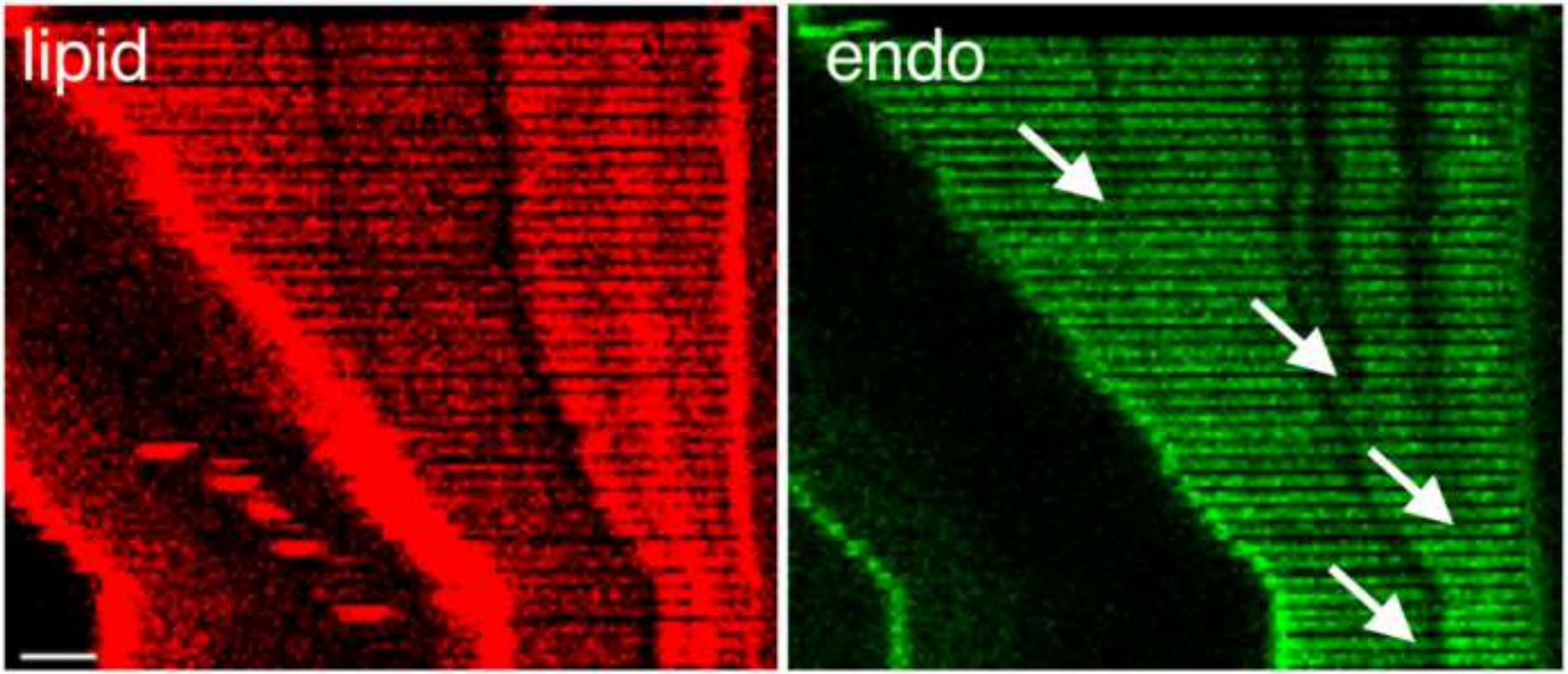

Supplemental Figure 5

Click here to download Supplemental Figure FigureS5.png

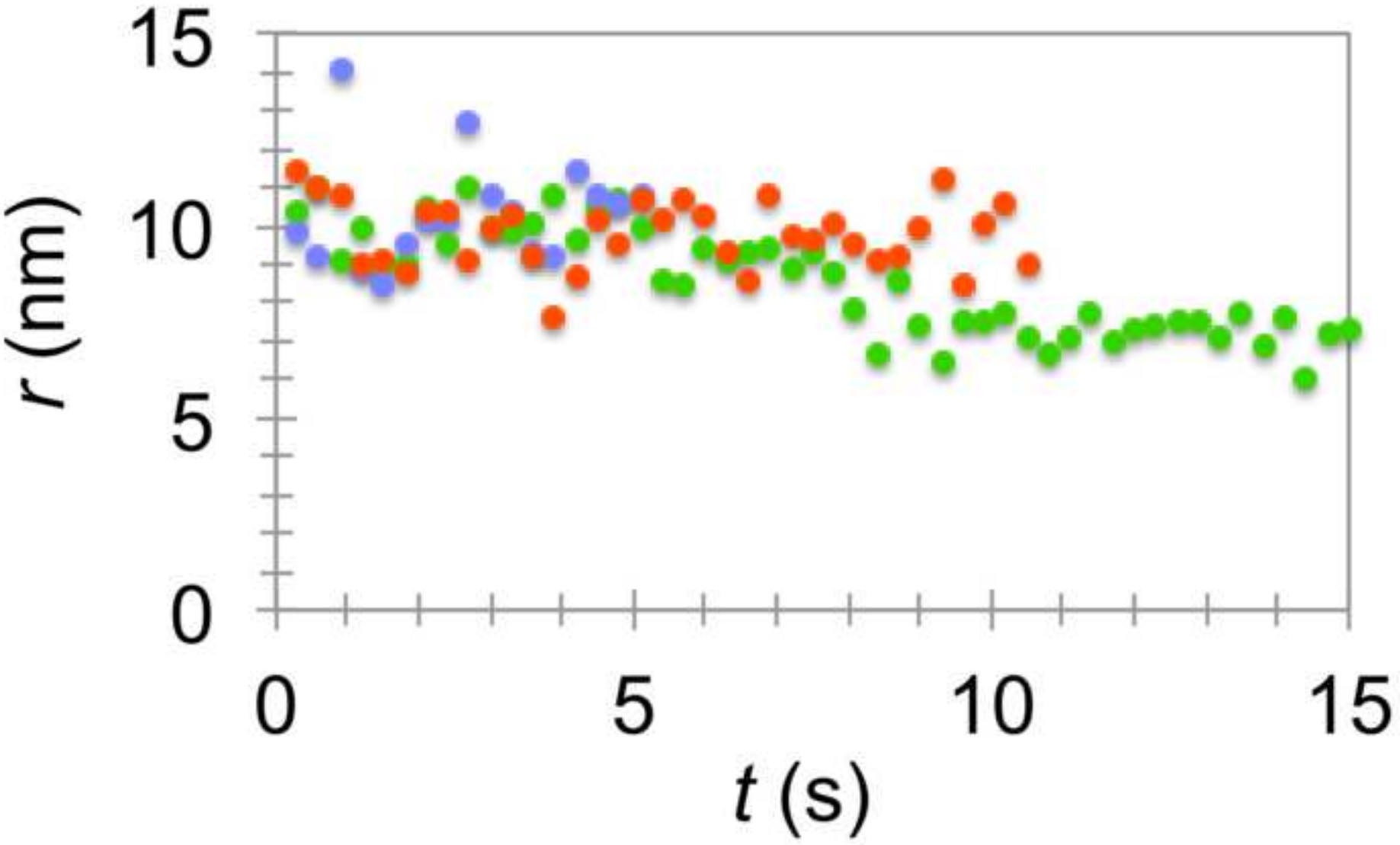

Supplemental Figure 6

Click here to download Supplemental Figure FigureS6.png

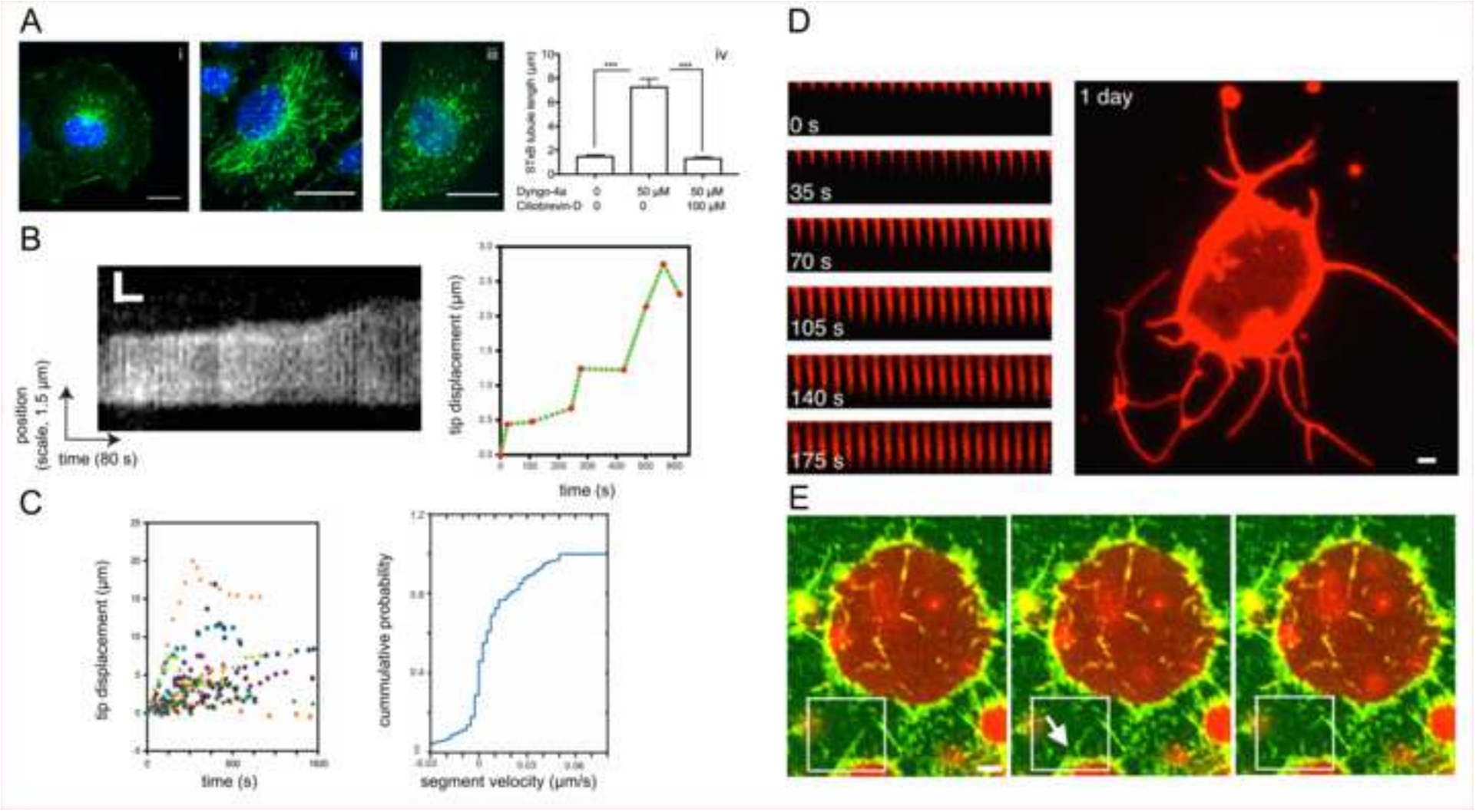

Supplemental Movie 1

Click here to access/download

Supplemental Movies and Spreadsheets

MovieS1.avi

Supplemental Movie 2

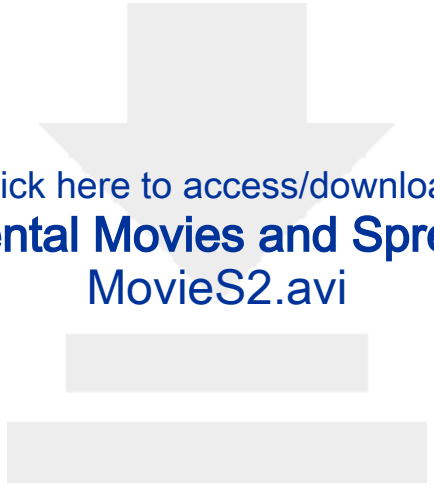

Click here to access/download

Supplemental Movies and Spreadsheets

MovieS2.avi

Click here to access/download

Supplemental Movies and Spreadsheets

MovieS3.avi

Supplemental Movie 4

Click here to access/download

Supplemental Movies and Spreadsheets

MovieS4.avi

Supplemental Movie 5

Click here to access/download

Supplemental Movies and Spreadsheets

MovieS5.avi